NMR-based diffusion pore imaging

Frederik Bernd Laun,[1,2] Tristan Anselm Kuder,[1] Andreas Wetscherek,[1] Bram Stieltjes,[2] and Wolfhard Semmler[1]
[1]*Medical Physics in Radiology, German Cancer Research Center (DKFZ), Im Neuenheimer Feld 280, 69120 Heidelberg, Germany*
[2]*Quantitative Imaging-Based Disease Characterization, German Cancer Research Center (DKFZ), Im Neuenheimer Feld 280, 69120 Heidelberg, Germany*

(Received 9 January 2012; revised manuscript received 23 May 2012; published 7 August 2012)

Nuclear magnetic resonance (NMR) diffusion experiments offer a unique opportunity to study boundaries restricting the diffusion process. In a recent Letter [Phys. Rev. Lett. **107**, 048102 (2011)], we introduced the idea and concept that such diffusion experiments can be interpreted as NMR imaging experiments. Consequently, images of closed pores, in which the spins diffuse, can be acquired. In the work presented here, an in-depth description of the diffusion pore imaging technique is provided. Image artifacts due to gradient profiles of finite duration, field inhomogeneities, and surface relaxation are considered. Gradients of finite duration lead to image blurring and edge enhancement artifacts. Field inhomogeneities have benign effects on diffusion pore images, and surface relaxation can lead to a shrinkage and shift of the pore image. The relation between boundary structure and the imaginary part of the diffusion weighted signal is analyzed, and it is shown that information on pore coherence can be obtained without the need to measure the phase of the diffusion weighted signal. Moreover, it is shown that quite arbitrary gradient profiles can be used for diffusion pore imaging. The matrices required for numerical calculations are stated and provided as supplemental material.

DOI: 10.1103/PhysRevE.86.021906 PACS number(s): 87.64.kj, 82.56.Lz

I. INTRODUCTION

In his seminal paper about spin echoes, Hahn already realized that diffusion of spins has a huge impact on the obtained nuclear magnetic resonance (NMR) signal [1], and soon afterwards, Carr and Purcell proposed two methods to extract the diffusion coefficient from the NMR signal [2]. One method, which is still widely used to date, was introduced by Stejskal and Tanner in 1965: the pulsed gradient method [3]. The essence of this method can be appreciated by considering the fundamental relation between applied main magnetic field B_0 and Larmor rotation frequency ω of spin packets in this field (see, e.g., Refs. [4,5]),

$$\omega = \gamma B_0, \tag{1}$$

where γ is the gyromagnetic ratio. In NMR imaging, in order to imprint spatial information, the main magnetic field is usually varied by applying additional gradient fields $\mathbf{G}$ for a certain time t, such that the total magnetic field $B = B_0 + \mathbf{G}\cdot\mathbf{x}$ becomes dependent on the position $\mathbf{x}$ of the nucleus [6]. Consequently, also the Larmor frequency $\omega = \gamma(B_0 + \mathbf{G}\cdot\mathbf{x})$ and the phase $\varphi = \omega t$ become space dependent. Thus, "frequency encoding" can be performed by measuring the signal while a gradient is applied, and "phase encoding" can be performed by measuring the signal after application of a gradient. Both methods are commonly used and yield the signal intensity at position $\mathbf{x}$ and thus an NMR image.

To measure free diffusion, Stejskal and Tanner [3] proposed to apply two consecutive gradients $\mathbf{G}_1$ and $\mathbf{G}_2 = -\mathbf{G}_1$ of equal duration $t_1 = t_2$. Suppose for simplicity that the gradients are applied for a duration that is much shorter than the relevant time scale of diffusive motion. Moreover, assume that there is a time gap between the gradients, in which the particle travels from $\mathbf{x}_1$ to $\mathbf{x}_2$. Then, when choosing a reference frame that rotates with $\omega = \gamma B_0$, the total particle phase is

$$\varphi = \gamma t_1 \mathbf{G}_1\cdot\mathbf{x}_1 + \gamma t_2 \mathbf{G}_2\cdot\mathbf{x}_2 = \gamma t_1 \mathbf{G}_1\cdot(\mathbf{x}_1 - \mathbf{x}_2). \tag{2}$$

Thus the phase encodes the displacement. The exact magnitude of the displacement $\Delta\mathbf{x} = \mathbf{x}_1 - \mathbf{x}_2$ is a random variable which depends on the diffusive motion. Consequently, the spin ensemble exhibits a phase dispersion. This dispersion leads to a signal loss which can be linked directly to the free diffusion constant D if no boundaries are present.

Much more interesting, however, is the case when the diffusion is restricted by boundaries [7]. The boundaries restrict the diffusive motion, such that the measurement of diffusion by NMR permits inferences on the shape of the boundaries. In most publications, information about boundaries is inferred from the reduction of the measured apparent diffusion coefficients due to boundaries (see, e.g., Refs. [8–11]). This approach yields impressive results, particularly in medical imaging. Axonal tracts induce a diffusion anisotropy which can be measured and used to reconstruct nerve fiber tracts in great detail [12–16]. Moreover, the diffusion anisotropy can be used to characterize many diseases such as, e.g., traumatic spinal cord injuries [17–19] or cancer [20,21]. In particular, the scalar apparent diffusion coefficient found in isotropic tissues is a powerful predictor of tissue integrity, which is used routinely in clinical stroke diagnosis [22,23], and in many tumor studies [24,25].

Beyond this intuitive level, many authors found more sophisticated links between the defining boundary and the diffusion process, in particular, considering the forward problem: Given a particular boundary, what is the diffusion weighted signal measured by a particular NMR diffusion experiment? This complicated problem was already addressed by early investigators such as Stejskal, Robertson, and Neumann and by many authors afterwards [7,26,27]. A particular comprehensive summary on this issue was recently written by Grebenkov [28].

While the forward problem is already complicated, the inverse problem is even more challenging. Nonetheless, many interesting discoveries have been made in the 60 years since Hahn's spin echo paper. One particularly compelling example

is that the surface-to-volume ratio S/V can be extracted from NMR diffusion experiments [29]. If boundaries are present, the diffusion coefficient $D(t) = \langle \Delta \mathbf{x}^2 \rangle / 6/t$ depends on the diffusion time t. The brackets denote the expectation value of all possible squared displacements. At very short diffusion times, $D(t)$ is approximately equal to the free diffusion constant D since most particles are not influenced by the boundaries. As time progresses, more and more particles bounce against the boundary and $D(t)$ decreases. The striking property of $D(t)$ is that there exists a universal behavior in the short time limit that does not depend on the exact shape of the boundary:

$$D(t) = D\left(1 - \frac{4}{9\sqrt{\pi}} \frac{S}{V} \sqrt{Dt} + \text{terms linear in } t\right). \quad (3)$$

Thus, by measuring $D(t)$ at different diffusion times, the surface-to-volume ratio S/V can be determined. In practice, this experiment is often difficult to perform since the diffusion must be measured at short diffusion times, but some advanced NMR techniques have been proposed to circumvent this limitation [30,31].

One important property of NMR diffusion measurements is that one needs to distinguish between the diffusion coefficient $D(t)$ and the coefficient $D_{\text{NMR}}(t)$ that is measured in NMR diffusion experiments. It can be shown (see, e.g., Ref. [32]) that $D_{\text{NMR}}(t) = D(t)$ if very short diffusion gradients are applied ($t_1 = t_2$ very short), but, in general, $D_{\text{NMR}}(t)$ is different from $D(t)$. For instance, $D_{\text{NMR}}(t)$ depends on t_1 and t_2 and on the time between the bipolar gradients. This complicates matters, but renders the NMR diffusion experiment richer and more fruitful. This becomes especially prominent when large gradient amplitudes are applied such that the quantity $\mathbf{q} = \gamma t_1 \mathbf{G}_1$, which is a wave-vector, becomes large. "Large" could, for example, mean $|\mathbf{q}| \gg L^{-1}$, with L being the characteristic length of the domain, e.g., the radius of a cylinder. If the condition $DT \gg L^2$ is fulfilled, then, as reported by Callaghan *et al.* and by Cory and Garroway in the beginning of the 1990s, the NMR diffusion experiment can be shown to be analogous to scattering experiments, e.g., x-ray scattering, in many regards (in this paper, we use the common label "q-space imaging" for this technique) [5,33,34]. In particular, the Fourier transform of the pore space function $\chi(\mathbf{x})$, which is 1 inside the domain and 0 outside, is analogous to the form factor. A similar problem arises: Using q-space imaging, only the power spectrum of $\chi(\mathbf{x})$ can be measured using bipolar diffusion gradients, and not the phase spectrum, such that an unambiguous determination of $\chi(\mathbf{x})$ is not possible.

This work, and the accompanying Letter [35], were motivated by the following question, which was in particular raised by Grebenkov in full clarity [28]: Is there any way to detect $\chi(\mathbf{x})$ using NMR diffusion experiments, and, if so, can this be translated in an applicable measurement technique?

The time-dependent diffusion coefficient $D(t)$ alone cannot reveal the exact shape of the boundary, which is essentially equivalent to the impossibility to infer the shape of a drum by hearing it [36,37]. However, the scattering-like properties of the q-space imaging technique generated some hope that this could be different for NMR diffusion experiments. This paper and the accompanying Letter [35] present the solution to this problem: the diffusion pore imaging technique, which allows to detect $\chi(\mathbf{x})$ of a single pore or an average $\chi(\mathbf{x})$ if a pore ensemble is measured. If the considered measurement volume contains many pores of similar shape, the center of mass of each pore appears to be shifted to the same location, resulting in an average pore shape in the final image. The measurement of pore ensembles is beneficial in comparison to microscopic MR imaging [5] since the signal of all pores is used for one single image, resulting in an effectively higher signal-to-noise (SNR) ratio, while the signal is spread out over the whole ensemble in microscopic MR imaging. In this paper, we give a detailed description of the diffusion pore imaging technique, thoroughly investigate occurring artifacts, and provide all matrices that are necessary to replicate the shown simulations. Moreover, the relation between boundary structure and the imaginary part of the diffusion weighted signal—which is only nonzero if the gradient profile is not temporally antisymmetric—is analyzed.

II. DIFFUSION PORE IMAGING: THE BASIC PRINCIPLE

In this section, we basically restate the findings of our recent Letter [35] for convenience and to clarify notation. The standard approach in diffusion NMR is to set $\mathbf{G}_1 = -\mathbf{G}_2$ and $t_1 = t_2$. Here, we investigate gradient settings in which $\mathbf{G}_1$ deviates from $\mathbf{G}_2$, while $\mathbf{G}_1 t_1 = -\mathbf{G}_2 t_2$ is fulfilled.

We first adapt the results that Mitra and Halperin [38] obtained for the case $\mathbf{G}_1 = -\mathbf{G}_2$. Assuming that a time-dependent magnetic field gradient $\mathbf{G}(t)$ is applied, a random walker acquires the phase

$$\varphi = \gamma \int \mathbf{G}(t) \cdot \mathbf{x}(t) dt \quad (4)$$

in the rotating reference frame. $\mathbf{x}(t)$ is the particle position at time t. Equation (4) is the generalization of Eq. (2). The transversal magnetization vector $\mathbf{M} = (M_x, M_y)^T$ is often expressed by the complex magnetization $M_{xy} = M_x + iM_y$, since this allows to express the signal attenuation S by

$$M_{xy} \propto S = \langle \exp(-i\varphi) \rangle = \left\langle \exp\left(-i\gamma \int_0^T \mathbf{G}(t) \cdot \mathbf{x}(t) dt\right) \right\rangle, \quad (5)$$

where $\langle \cdot \rangle$ denotes an average over all random walks. We define the temporal gradient profiles $\mathbf{G}_{t_1,t_2,T}(t)$ by

$$\mathbf{G}_{t_1,t_2,T}(t) = \mathbf{G} \cdot \begin{cases} -1 & \text{for } 0 < t < t_1, \\ t_1/t_2 & \text{for } T - t_2 < t < T, \\ 0 & \text{otherwise.} \end{cases} \quad (6)$$

Here, T is the total duration of the temporal gradient profile, and t_1 and t_2 are the durations of first and second gradient. By this definition, it is ensured that the zeroth moment is zero,

$$\int_0^T \mathbf{G}_{t_1,t_2,T}(t) dt = 0. \quad (7)$$

This is called the rephasing condition and ensures that particles that do not change position acquire no net phase [see Eqs. (2) and (4)]. The q value is defined by the magnitude q of the vector $\mathbf{q} = \gamma \mathbf{G} t_1$. Using the temporal gradient profile

$\mathbf{G}_{t_1,t_2,T}(t)$, Eq. (5) can be expressed as

$$S(\mathbf{q}) = \left\langle \exp\left[i\mathbf{q} \cdot \left(\frac{1}{t_1} \int_0^{t_1} \mathbf{x}(t)dt - \frac{1}{t_2} \int_{T-t_2}^{T} \mathbf{x}(t)dt \right) \right] \right\rangle. \quad (8)$$

The integral $\frac{1}{t_1} \int_0^{t_1} \mathbf{x}(t)dt$ can be interpreted as the center of mass of the random walk trajectory ranging from $\mathbf{x}(0)$ to $\mathbf{x}(t_1)$ [38]. Introducing the centers of mass of the individual random walk trajectories

$$\mathbf{x}_{\text{c.m.},1} = \frac{1}{t_1} \int_0^{t_1} \mathbf{x}(t)dt \quad (9)$$

and

$$\mathbf{x}_{\text{c.m.},2} = \frac{1}{t_2} \int_{T-t_2}^{T} \mathbf{x}(t)dt, \quad (10)$$

Eq. (8) becomes

$$S(\mathbf{q}) = \langle \exp[i\mathbf{q} \cdot (\mathbf{x}_{\text{c.m.},1} - \mathbf{x}_{\text{c.m.},2})] \rangle. \quad (11)$$

In the case of finite gradient duration, this equation cannot be directly related to the diffusion propagator, but to a center of mass (COM) propagator $P_{\text{COM}}(\mathbf{x}_{\text{c.m.},1}, \mathbf{x}_{\text{c.m.},2})$, which describes the probability that a trajectory during the first gradient with $\mathbf{x}_{\text{c.m.},1}$ results in a trajectory during the second gradient with $\mathbf{x}_{\text{c.m.},2}$. The signal attenuation is connected to the *trajectory* displacements through the wave vector $\mathbf{q}$ and can be used to measure this voxel-averaged center of mass propagator as described in Ref. [38].

Previously, the limit of short gradient durations t_1 and $t_1 = t_2$ has been investigated extensively (e.g., Refs. [5,7,33,39–42]). Experiments using such short gradient pulses are usually labeled "q-space imaging" experiments. In this limit, $\mathbf{x}_{\text{c.m.},1}$ and $\mathbf{x}_{\text{c.m.},2}$ are approximately equal to the initial and final particle positions $\mathbf{x}_1$ and $\mathbf{x}_2$. Hence, Eq. (11) becomes

$$S(\mathbf{q}) = \langle \exp[i\mathbf{q} \cdot (\mathbf{x}_1 - \mathbf{x}_2)] \rangle = \langle \exp[i\mathbf{q} \cdot \mathbf{x}_1] \exp[-i\mathbf{q} \cdot \mathbf{x}_2] \rangle . \quad (12)$$

The signal attenuation is connected to the *particle* displacements through the wave vector $\mathbf{q}$ and can be used to measure the voxel-averaged diffusion propagator as described, e.g., in Refs. [7,42]. For the short gradient pulses considered here, the center of mass propagator becomes the well-known diffusion propagator.

Further assuming that the diffusion process is in the long time limit (or in the so-called motional narrowing regime), the final particle position can be anywhere within the closed pore with equal probability, independently of the starting position. Hence,

$$\begin{aligned} &\langle \exp[i\mathbf{q} \cdot \mathbf{x}_1] \exp[-i\mathbf{q} \cdot \mathbf{x}_2] \rangle \\ &= \frac{1}{V^2} \int_\Omega d\mathbf{x}_1 \exp(i\mathbf{q} \cdot \mathbf{x}_1) \int_\Omega d\mathbf{x}_2 \exp(-i\mathbf{q} \cdot \mathbf{x}_2) \\ &= \frac{1}{V^2} \tilde{\chi}^*(\mathbf{q}) \tilde{\chi}(\mathbf{q}) = \frac{1}{V^2} |\tilde{\chi}^2(\mathbf{q})|. \end{aligned} \quad (13)$$

Here, the integration is performed over the domain Ω, in which $\chi(\mathbf{x})$ is equal to one. Thus, it is possible to measure the power spectrum of the pore space function, but, as in many scattering experiments, the inverse Fourier transform cannot be performed since the phase information is lost [5,33,43]. The quantity $\tilde{\chi}(\mathbf{q})$ is the analogue of the form factor.

In diffusion NMR, the loss of the phase information is a direct consequence of the antisymmetry $\mathbf{G}_{t_1,t_1,T}(t) = -\mathbf{G}_{t_1,t_1,T}(T-t)$ of the temporal gradient profile [28,44]. As we show in the following, the phase information of the signal can be preserved if the temporal gradient profile $\mathbf{G}_{t_1,t_2,T}(t)$ is used and if $t_1 \neq t_2$. First, we consider the temporal gradient profile $\mathbf{G}_{t_1 \approx T, t_2 \ll T, T}(t)$ for which t_1 is approximately equal to T and t_2 is very short. Then, the signal is

$$S(\mathbf{q}) = \langle \exp[i\mathbf{q} \cdot (\mathbf{x}_{\text{c.m.},1} - \mathbf{x}_2)] \rangle. \quad (14)$$

Thus, the signal attenuation is connected to the distance $\mathbf{x}_{\text{c.m.},1} - \mathbf{x}_2$ by the wave vector $\mathbf{q}$ and can be used to measure a voxel-averaged center of mass propagator. Here, this propagator describes the probability that a trajectory with center of mass $\mathbf{x}_{\text{c.m.},1}$ ends at position $\mathbf{x}_2$ [7,42].

For closed domains and long gradient duration, the particle was at every position within the boundary with an equal probability. Thus,

$$\mathbf{x}_{\text{c.m.},1} = \mathbf{x}_{\text{c.m.}}, \quad (15)$$

where $\mathbf{x}_{\text{c.m.}}$ is the center of mass of the pore space function $\chi(\mathbf{x})$ of a closed domain.

In the long-time limit, Eq. (14) becomes

$$\begin{aligned} S(\mathbf{q}) &= \langle \exp[i\mathbf{q} \cdot (\mathbf{x}_{\text{c.m.}} - \mathbf{x}_2)] \rangle \\ &= \frac{1}{V} \exp[i\mathbf{q} \cdot \mathbf{x}_{\text{c.m.}}] \int_\Omega d\mathbf{x}_2 \exp(-i\mathbf{q} \cdot \mathbf{x}_2) \\ &= \frac{1}{V} \exp[i\mathbf{q} \cdot \mathbf{x}_{\text{c.m.}}] \tilde{\chi}(\mathbf{q}). \end{aligned} \quad (16)$$

Thus the pore space function can be determined exactly by inverse Fourier transformation [see Fig. 1(a)].

For a second identical pore that is shifted by $\Delta\mathbf{x}_s$, $\mathbf{x}_{\text{c.m.}}$ becomes $\mathbf{x}_{\text{c.m.}} + \Delta\mathbf{x}_s$, and $\mathbf{x}_2$ becomes $\mathbf{x}_2 + \Delta\mathbf{x}_s$. Thus the signal

$$\begin{aligned} S(\mathbf{q}) &= \langle \exp\{i\mathbf{q} \cdot [(\mathbf{x}_{\text{c.m.}} + \Delta\mathbf{x}_s) - (\mathbf{x}_2 + \Delta\mathbf{x}_s)]\} \rangle \\ &= \langle \exp[i\mathbf{q} \cdot (\mathbf{x}_{\text{c.m.}} - \mathbf{x}_2)] \rangle \end{aligned} \quad (17)$$

is identical to that of the nonshifted pore. If the second pore is shaped differently, the obtained image is the average of the two pore space functions.

These findings can be interpreted as follows: If the first gradient is applied for a sufficiently long time, the random walker acquires a phase identical to that of a particle located at the center of mass of the domain. On the other hand, the second gradient is too short for diffusion dynamics to be of any importance. It merely produces a linear phase dispersion, as does an ordinary NMR imaging gradient [4,5]. Therefore, the experiment feigns to be a diffusion experiment, but it is actually an imaging experiment in disguise: The dynamics are completely lost. Hence, it follows naturally that the diffusion-weighted signal may bear a phase just as the signal does in standard magnetic resonance imaging. This allows acquiring images of closed pores, and thereby the unambiguous detection of the pore space function.

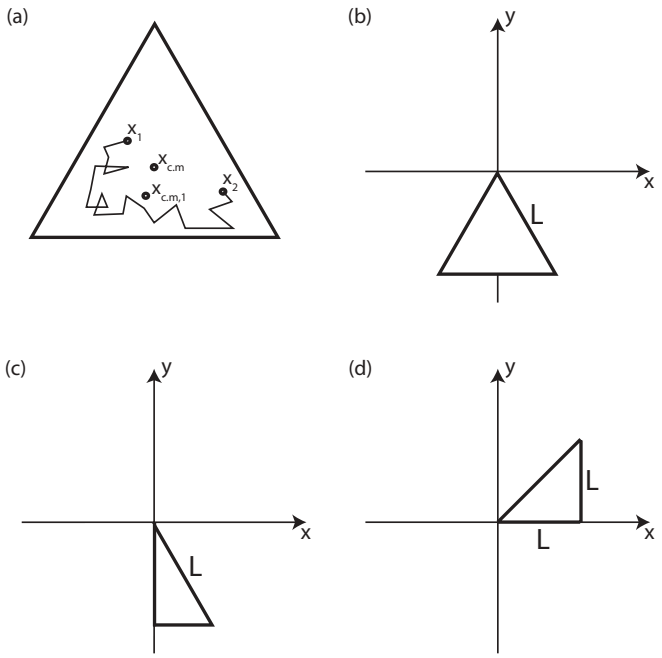

FIG. 1. (a) Basic idea of the diffusion pore imaging technique. A particle travels from x_1 to x_2 in a closed domain. The long gradient ensures that the particle obtains the phase corresponding to the center of mass $x_{\mathrm{c.m.},1}$ of the trajectory. The second gradient imprints the phase corresponding to the final particle position x_2. As the experiment averages over all possible random walks, a probability function (or propagator) is measured, which indicates the probability that a trajectory occurs with center of mass $x_{\mathrm{c.m.}1}$ and final position x_2. In the long-time limit, $x_{\mathrm{c.m.},1}$ is approximately equal to the center of mass $x_{\mathrm{c.m.}}$ of the domain, $x_{\mathrm{c.m.},1}$ and x_2 are not correlated any more, and the final particle position x_2 is anywhere in the domain with equal probability. Thus, the diffusion pore imaging experiment essentially measures the probability that a particle ends up at $x_2 - x_{\mathrm{c.m.}}$. The spatial profile of this probability allows one to retrieve the shape of the pore: It is zero outside the pore and nonvanishing inside the pore. (b)–(d) Three model domains for which the matrices $\mathcal{B}$ were computed. L is the length of the annotated edges. (b) Equilateral triangle. (c) Hemiequilateral triangle. (d) Perpendicular isosceles triangle.

III. THE MCF TECHNIQUE: A TOOL FOR SIMULATIONS AND THEORETICAL ANALYSIS

In the following sections, numerical simulations and theoretical analyses are presented that are based on the multiple correlation function (MCF) technique. It was used since it offers clear theoretical insights and very efficient numerical calculations. It is somewhat similar to the multiple propagator technique [45,46], and relies on a series expansion of the transversal magnetization in eigenfunctions $u_n(\mathbf{r})$ of the Laplace operator. The MCF technique was introduced by Barzykin [47] and was worked out in detail by Axelrod and Sen [48] and in particular by Grebenkov [28]. In this paper we follow the notation of Grebenkov. This section is included for convenience and to clarify the notation, it states equations and findings that are important to understand Sec. IV.

We start from the Bloch-Torrey equation, which describes the evolution of the normalized, complex transverse magnetization $\mathfrak{m}(\mathbf{r},\mathrm{t}) = \mathfrak{m}_x(\mathbf{r},\mathrm{t}) + i\mathfrak{m}_y(\mathbf{r},\mathrm{t})$ when a gradient field $\mathbf{G}$ of amplitude $G = |\mathbf{G}|$ is applied and when diffusion is present [49]:

$$\left(\frac{\partial}{\partial t} - D\Delta + i\gamma\mathbf{G}\cdot\mathbf{r}\right)\mathfrak{m}(\mathbf{r},\mathrm{t}) = 0. \tag{18}$$

The magnetization $\mathfrak{m}(\mathbf{r},\mathrm{t})$ is normalized such that the signal attenuation S is initially equal to one:

$$S = \int_\Omega \mathfrak{m}(\mathbf{r},0)\,d\mathbf{r} = 1. \tag{19}$$

It is first assumed that $\mathbf{G}$ is constant in time, a restriction that is omitted later. D is the free diffusion coefficient. Now, $\mathfrak{m}(\mathbf{r},t)$ is expanded in eigenfunctions $u_n(\mathbf{r})$ of the Laplace operator:

$$\mathfrak{m}(\mathbf{r},t) = \sum_{n=0}^{\infty} c_n(t)u_n(\mathbf{r}). \tag{20}$$

Substituting this expression in the Bloch-Torrey equation, multiplying by $u_m^*(\mathbf{r})$, and integrating over the domain yields

$$\left(\frac{d}{dt}c_m(t) + \frac{D\lambda_m}{L^2}c_m(t) + i\gamma LG\sum_{n=0}^{\infty}\mathcal{B}_{m,n}c_n(t)\right) = 0, \tag{21}$$

with

$$\mathcal{B}_{m,n} = \frac{1}{LG}\int_\Omega u_m^*(\mathbf{r})u_n(\mathbf{r})\mathbf{G}\cdot\mathbf{r}d\mathbf{r}. \tag{22}$$

Note that the eigenfunctions satisfy $\Delta u_m(\mathbf{r}) = -(\frac{\lambda_m}{L^2})u_m(\mathbf{r})$ with the dimensionless eigenvalues λ_m. The parameter L is the typical length scale of the domain (e.g., the radius of a cylinder). The eigenfunctions fulfill the boundary condition $\frac{\partial}{\partial n}u_m(\mathbf{r}) + hL^{-1}u_m(\mathbf{r}) = 0$, where $\frac{\partial}{\partial n}$ denotes the derivative perpendicular to the boundary and h is the dimensionless surface relaxivity. It is connected to the surface relaxivity ρ by $h = \rho L/D$. The eigenfunctions are directly related to the diffusion propagator $P(\mathbf{r},\mathbf{r}',t)$ by

$$P(\mathbf{r},\mathbf{r}',t) = \sum_{m=0}^{\infty} u_m(\mathbf{r})u_m^*(\mathbf{r}')\exp(-Dt\lambda_m/L^2). \tag{23}$$

Equation (21) can be solved,

$$\mathbf{C}(t) = e^{-(p\Lambda + iq_G\mathcal{B})t/T}\mathbf{C}(0), \tag{24}$$

where $\mathbf{C}(t)$ is a vector containing the components $c_m(t)$. The matrix Λ is a diagonal matrix with elements $\Lambda_{m,n} = \delta_{m,n}\lambda_m$. Moreover, the dimensionless parameters $p = \frac{DT}{L^2}$ and $q_G = \gamma GTL$ were introduced.

In order to compute the coefficients $c_m(t)$, the initial transversal magnetization $\mathfrak{m}(\mathbf{r},t=0)$ must be specified by a vector $c_m(t=0)$. We assume that $\mathfrak{m}(\mathbf{r},t=0)$ is homogeneous. If $h = 0$, the zeroth eigenvalue is $\lambda_0 = 0$ and $u_0(\mathbf{r}) = V^{-1/2}$, where V is the volume of the domain Ω. Then the coefficients $c_m(0)$ are $c_m(0) = V^{-1/2}\delta_{0,m}$. The factor $V^{-1/2}$ in this expression was introduced to guarantee a dimensionless signal attenuation in Eq. (26), such that $S = 1$ at time $t = 0$. To get rid of the $V^{-1/2}$ factor, the dimensionless vector $\mathbf{U} = V^{1/2}\mathbf{C}(0)$ is introduced, which has components U_m.

If $h \neq 0$, the coefficients $c_m(0)$ must be computed according to

$$c_m(0) = V^{-1} \int_\Omega u_m(\mathbf{r}) d\mathbf{r}. \tag{25}$$

Assuming that the detection coil has a homogeneous sensitivity profile, the signal attenuation is equal to the integral of $\mathfrak{m}(\mathbf{r},t)$ over the domain:

$$\begin{aligned} S &= \int_\Omega \mathfrak{m}(\mathbf{r},t) d\mathbf{r} = \sum_{n=0}^{\infty} c_n(t) \int_\Omega u_n(\mathbf{r}) d\mathbf{r} \\ &= V \sum_{n=0}^{\infty} c_n(t) c_n(0). \end{aligned} \tag{26}$$

Hence, if no surface relaxation is present, the signal attenuation is

$$\begin{aligned} S &= V \mathbf{C}^\dagger(0) e^{-(p\Lambda + iq_G\mathcal{B})t/T} \mathbf{C}(0) = \mathbf{U}^\dagger e^{-(p\Lambda + iq_G\mathcal{B})t/T} \mathbf{U} \\ &= [e^{-(p\Lambda + iq_G\mathcal{B})t/T}]_{0,0}. \end{aligned} \tag{27}$$

The subscript 0,0 denotes the first diagonal element of the matrix $\exp[-(p\Lambda + iq_G\mathcal{B})t/T]$. If surface relaxation is present, the signal attenuation must be normalized using the signal without diffusion gradient

$$S = \frac{\mathbf{U}^\dagger e^{-(p\Lambda + iq_G\mathcal{B})t/T} \mathbf{U}}{\mathbf{U}^\dagger e^{-p\Lambda t/T} \mathbf{U}}. \tag{28}$$

This is a valuable expression to compute the signal attenuation, since knowledge of Λ and $\mathcal{B}$ allows the straightforward computation of S using mathematical software such as MATLAB (MathWorks, Natick, MA, USA).

In diffusion NMR, the gradient profile is time dependent, thus $\mathbf{G}$ becomes $\mathbf{G}(t)$. Equations (27) and (28) can be generalized straightforwardly if $\mathbf{G}(t)$ is piecewise constant. For example, Eq. (27) becomes

$$\begin{aligned} S = \{&\exp[-(p\Lambda + iq_G\mathcal{B}t_1/t_2)t_2/T] \\ &\times \exp[-p\Lambda(T - t_1 - t_2)/T] \exp[-(p\Lambda - iq_G\mathcal{B})t_1/T]\}_{0,0} \end{aligned} \tag{29}$$

for the gradient profile $\mathbf{G}_{t_1,t_2,T}(t)$ defined in Eq. (6). An alternative approach is to expand Eq. (5) in φ if φ is small (e.g., moderate diffusion weighting):

$$S = \langle e^{-i\varphi} \rangle \approx 1 - i\langle \varphi \rangle - \tfrac{1}{2}\langle \varphi^2 \rangle. \tag{30}$$

The linear term $\langle \varphi \rangle$ is zero because of the rephasing condition (7). By expanding Eq. (27) in q_G (see Refs. [28] and [48]), $\langle \varphi^2 \rangle$ can be expressed by

$$\langle \varphi^2 \rangle = 2q_G^2 \sum_{m=0}^{\infty} \mathcal{B}_{0,m}^2 \int_0^1 d\tau_1 \int_{\tau_1}^1 d\tau_2 f(\tau_1) f(\tau_2) e^{p\lambda_m(\tau_1 - \tau_2)}, \tag{31}$$

where surface relaxivity is assumed to be zero, and where the normalized effective temporal gradient profile $f(\tau) = |\mathbf{G}(\tau T)|/G$ was introduced. For example,

$$f_{\delta_1,\delta_2}(\tau) = \begin{cases} -1 & \text{for } 0 < \tau < \delta_1, \\ \delta_1/\delta_2 & \text{for } (1-\delta_2) < \tau < 1, \\ 0 & \text{otherwise,} \end{cases} \tag{32}$$

with $\delta_1 = t_1/T$ and $\delta_2 = t_2/T$. The time parameter τ is dimensionless.

We further use the discrete gradient profile

$$\begin{aligned} f_{\text{An Die Freude}} = &-66/166(3,3,4,5,5,4,3,2,1,1,2,3,3,2,2,2, \\ &3,3,4,5,5,4,3,2,1,1,2,3,2,1,1,1, \\ &-163,2,2,3,1,2,3,4,3,1,2,3,4,3,2,1,2, \\ &-2,3,3,4,5,5,4,3,2,1,1,2,3,2,1,1,1)^T \end{aligned} \tag{33}$$

that consists of 66 equidistant time steps to show that diffusion pore imaging can be performed with quite arbitrary gradient profiles. It basically represents the fingering of Beethoven's musical interpretation of the ode "An die Freude" with one additional sharp gradient pulse (the value −163).

Equation (31) is a suitable starting point for further theoretical analysis. The contribution of each eigenfunction can be clearly appreciated, and if the effective temporal profile $f(\tau)$ is specified, the double integral in Eq. (31) can be performed explicitly. According to Grebenkov [28], in a first approximation, the exponential function in Eq. (31) can be replaced by $(p\lambda_m)^{-1}\delta(t_2 - t_1)$ in the motional narrowing regime (where $p = DT/L^2$ is large) using non-narrow temporal profiles. Thus, Eq. (31) can be written as

$$\langle \varphi^2 \rangle = 2q_G^2 p^{-1} \sum_{m=1}^{\infty} \mathcal{B}_{0,m}^2 \lambda_m^{-1} \int_0^1 d\tau f^2(\tau) + O(p^{-2}), \tag{34}$$

and hence

$$\langle \varphi^2 \rangle \approx 2q_G^2 p^{-1} \zeta_{-1} \int_0^1 d\tau f^2(\tau). \tag{35}$$

Thus the contribution of temporal profile [specified by $f(\tau)$] and eigensystem (specified by ζ_{-1}) decouple in the motional narrowing regime. $\zeta_{-1} = \sum_{m=1}^{\infty} \mathcal{B}_{0,m}^2 \lambda_m^{-1}$ is a domain-dependent, dimensionless constant. It is, e.g., 1/120 for the slab, 7/96 for the cylinder, and 2.2951×10^{-3} for the equilateral triangle if spatially linear gradients are used. Besides that, Eq. (31) is an important statement since the signal attenuation can often be well described by

$$S = \exp\left(-\tfrac{1}{2}\langle \varphi^2 \rangle\right). \tag{36}$$

This so-called Gaussian phase approximation is important since it is correct for free diffusion (with a Gaussian diffusion propagator), but also applicable to a wide range of experimental settings in diffusion NMR, for which the diffusion propagator is not necessarily Gaussian [28]. For example, it is valid for small φ, in the short time limit, or in the motional narrowing regime using long diffusion gradients [27,28,50].

The simulations in Sec. VI were performed by implementing Eqs. (27)–(29) in MATLAB. The required matrices were truncated in size. The sufficiency of the used number of eigenvalues was ensured by comparing the results to computations with an increased number of eigenvalues. The MCF approach is mainly useful for closed domains. If the domain is open, or has many separated length scales, the number of eigenvalues that are required for a reliable computation may become unfeasibly large. Further details on implementation issues can be found in Refs. [51,52]. The required matrices $\mathcal{B}$ have so far only been derived for highly

symmetric domains such as slab, cylinder, etc. [28,47,53–56], but not for domains of reduced symmetry, where, for example, a nonzero phase of the diffusion weighted signal attenuation can be observed. We therefore derived the required matrices of the equilateral triangle, the hemiequilateral triangle, and the isosceles perpendicular triangle [see Figs. 1(b)–1(d)]. These matrices and the eigenfunctions are stated in Appendixes A and B and are provided as Supplemental Material [57]. Some further results concerning the ζ constants of the isosceles triangle are stated in Appendix C. Interpreting the MCF approach as an imaging technique yields interesting insights into the relation between the $\mathcal{B}$ matrices and the shape of the domain. This is described in Appendix D. In Appendix E, the effect of 180° pulses on the effective temporal gradient profile $f(\tau)$, and some subtleties that do not arise when using antisymmetric profiles, are discussed.

IV. PORE IMAGING ARTIFACTS

In this section, we investigate several artifacts that may have an influence on the proposed diffusion pore imaging technique.

A. Gradient duration

In Sec. II, the ideal gradient configuration was assumed. The first gradient was assumed to be of infinite duration, while the second gradient was assumed to be infinitesimal. In Sec. IV A, we investigate the effect of deviations from this idealized situation.

1. First gradient finite: Blurring

If the first gradient is not infinitely long, $\mathbf{x}_{\mathrm{c.m.},1} = t_1^{-1}\int_0^{t_1}\mathbf{x}(t)dt$ is only approximately equal to the center of mass (COM) $\mathbf{x}_{\mathrm{c.m.}}$ of the domain [see Eq. (15)]. If the gradient, although not being infinitely long, is long in the sense that $t_1 D/L^2 \gg 1$, we can safely assume that the Gaussian phase approximation holds (see Ref. [28] and references therein), and hence the distribution of $\mathbf{x}_{\mathrm{c.m.},1}$ must be Gaussian. Mitra and Halperin [38] and de Swiet [58] showed in particular that $\mathbf{x}_{\mathrm{c.m.},1}$ is distributed as a Gaussian function for the slab geometry. The Gaussian phase approximation is appropriate since $\mathbf{x}_{\mathrm{c.m.},1} = t_1^{-1}\int_0^{t_1}\mathbf{x}(t)dt$ can be interpreted as a sum of uncorrelated random variables in the long time limit, such that the central limit theorem guarantees that $\mathbf{x}_{\mathrm{c.m.},1}$ is distributed as a Gaussian function. This Gaussian function is centered around $\mathbf{x}_{\mathrm{c.m.}}$, becomes more narrow with increasing t_1, and converges towards a Dirac delta function for $t_1 \to \infty$. The width of the COM distribution at finite t_1 leads to a blurring of the pore image. The amount of blurring is determined by the width of the Gaussian function. To estimate this width, we take an approach similar to the one used by de Swiet [58], which, however, can be applied to arbitrary domains. We start with the expression given in Eq. (35), where the integral $I_f = \int f^2(\tau)d\tau$ must be calculated. For a constant first gradient [Eqs. (6) and (32)] and under the assumption that $t_1 \approx T$, one finds

$$I_f = \int_0^{t_1/T} d\tau f^2(\tau) \approx 1. \tag{37}$$

If the normalized temporal gradient profile $f_{\text{An Die Freude}}$ is used (without the sharp gradient pulse), one finds

$$I_f = \int_0^1 d\tau\, f^2_{\text{An Die Freude}}(\tau) \approx 1.3091, \tag{38}$$

which is larger than 1 and thus yields a slower convergence of $\mathbf{x}_{\mathrm{c.m.},1}$ towards $\mathbf{x}_{\mathrm{c.m.}}$ than the constant first gradient. The corresponding generalized expression $\mathbf{x}_{\mathrm{c.m.},1} = t_1^{-1}\int_0^{t_1} f(t)\mathbf{x}(t)dt$ can still be considered to be a weighted sum of uncorrelated random variables in the long time limit, thus entailing the validity of the Gaussian phase approximation.

Using Eqs. (37) and (38), Eq. (35) becomes

$$\langle\varphi^2\rangle = 2\gamma^2 G^2 T D^{-1} L^4 \zeta_{-1} I_f. \tag{39}$$

This expression is valid in the motional narrowing regime and describes the variance of the phase distribution. To find an expression for the standard deviation σ_x of the COM distribution, we set $x_{\mathrm{c.m.},1} = \varphi/\gamma GT$ and find

$$\sigma_x = \sqrt{\langle x^2_{\mathrm{c.m.},1}\rangle} = L^2\sqrt{\frac{2\zeta_{-1}I_f}{TD}}. \tag{40}$$

Thus the standard deviation of the COM distribution decreases with $T^{-1/2}$, but increases with L^2. In large domains, it takes a long time for the COM distribution to narrow down. The COM distribution is then given by

$$\left(2\pi\sigma_x^2\right)^{-1/2}\exp\left(-\frac{x^2_{\mathrm{c.m.},1}}{2\sigma_x}\right) \tag{41}$$

in one dimension. In two and three dimensions, the constant ζ_{-1} becomes "tensorial." For cylinder, sphere, and equilateral triangle, ζ_{-1} (and the diffusion tensor) is "spherical." The quantity $x_{\mathrm{c.m.},1}$ should be interpreted as the projection along the gradient direction. For example, for the equilateral triangle and constant first gradient, we find the numerical value $\sigma_x = 0.214\ \mu$m (with length of edges $L = 10\ \mu$m, $D = 1\ \mu\mathrm{m}^2/\mathrm{ms}$, and $T = 1$ s).

2. Second gradient finite: Edge enhancement

If the second gradient is not of infinitesimal duration, $\mathbf{x}_{\mathrm{c.m.},2} = \frac{1}{t_2}\int_{T-t_2}^{T}\mathbf{x}(t)\,dt$ is only approximately equal to $\mathbf{x}(t)$. Two special cases can be distinguished: the motional narrowing regime ($Dt_2 \gg L^2$) and the slow diffusion regime ($Dt_2 \ll L^2$). Here, we only consider the slow diffusion regime. Otherwise, if $Dt_2 \ll L^2$ is not fulfilled, the experiment cannot be regarded as an imaging experiment.

In the slow diffusion regime, non-narrow imaging gradients result in the edge enhancement effect that is well known from microscopic NMR imaging [58–62]. As pointed out by de Swiet [58], the edge enhancement effect differs for frequency encoding and phase encoding. The pore imaging technique relies completely on phase encoding, for which the following properties are observed. The intensity profile is approximately zero at the boundary, since the particle trajectory tends to push $\mathbf{x}_{\mathrm{c.m.},2}$ away from the boundary. In the bulk of the domain, it is not of importance whether $\mathbf{x}_{\mathrm{c.m.},2}$ is identical to $\mathbf{x}(t)$. It is only important if the distributions of $\mathbf{x}_{\mathrm{c.m.},2}$ and $\mathbf{x}(t)$ are identical, which is usually the case. Thus, since the integrated signal intensity should stay constant, and since it stays constant in

the bulk, while it is decreases at the boundary, there must exist some region close to the boundary of increased signal intensity. Mitra and Halperin empirically found that the intensity curve close to the boundary of a slab can be approximated by

$$\exp\left(-\frac{a}{x_s^2}\right)\{1+b\exp[-c(x_s+x_{s,0})^2]\}, \tag{42}$$

with the parameters $a=0.1181$, $b=7.703$, $c=0.6361$, and $x_{s,0}=1.206$ [38]. The scaled variable x_s is identical to $x_s = x_b/\sqrt{Dt_2}$, where x_b is the distance from the boundary. The peak of this distribution is at

$$x_{b,\max} = 0.5926\sqrt{Dt_2}. \tag{43}$$

As reported by de Swiet [58], using phase encoding, the signal at the peak can only be larger by a factor of 1.42, while this contrast can be arbitrarily large using frequency encoding.

3. *Impact on experimental settings*

We derive a rough estimate of the impact of finite gradients on experimental settings by relying on the slab domain, since Eq. (43) is applicable straightforwardly. Assume that the two plates are separated by L, and that an image of 10 pixels shall be acquired, such that the pixel size is $\Delta x_p = \pi q^{-1} = L/10$. The maximal obtainable q value is $q_{\max} = \gamma G_{\max} t_2$, given that the maximal gradient amplitude of the scanner is $G_{\max}$. It follows that the second gradient must be applied for the required time $t_{2,r} = \pi(\gamma G_{\max}\Delta x_p)^{-1}$ if the pixel size Δx_p shall be reached. Thus, the edge enhancement peak is at position [compare to Eq. (43)]

$$x_{b,\max} = 0.5926\sqrt{\frac{D\pi}{\gamma G_{\max}\Delta x_p}}. \tag{44}$$

The expression $x_{b,\max}/\Delta x_p$ quantifies the position of this peak in units of pixel sizes.

The width of the blurring caused by a finite first gradient is described by Eq. (40). As $\zeta_{-1} = 1/120$ for the slab domain, and $I_f \approx 1$, one finds $\sigma_x = L^2/\sqrt{60TD}$ if it is assumed that $t_1 \approx T$. Thus, the duration of the first gradient that is required so that $\sigma_x \leqslant \Delta x_p$ is $t_{1,r} \geqslant 1000\Delta x_p^2/6/D$.

Here, the following cases are considered: (1) Water diffusing in a cell with a typical diameter of 10 μm. (2) Water diffusing in a thin neuronal axon with a diameter of 1 μm (see, e.g., Chaps. 5 and 6 of Ref. [8]). (3) Water diffusing in a squid giant axon with a diameter of 500 μm [63]. (4) *N*-acetylaspartic acid (NAA) diffusing in the soma of a neuron with 10 μm diameter of the soma. (5) Gaseous xenon diffusing in lung alveoli. A typical diameter of lung alveoli is 200 μm [64]. (6) Some lung diseases such as chronic obstructive disease (COPD) cause a degeneration of lung tissue and can result in much larger alveoli diameters. An exemplary diameter of diseased alveoli of 1 mm is used.

Three different maximal gradient amplitudes $G_{\max}$ are considered: (1) $G_{\max} = 45$ mT/m, which is a typically available gradient amplitude on clinical whole body scanners (e.g., gradient system TQ-engine, Siemens Medical Solutions, Germany). (2) $G_{\max} = 1$ T/m, which is a gradient amplitude that is available on small animal scanners (e.g., BGA6-S gradient system, Bruker BioSpin, Germany). (3) $G_{\max} = 50$ T/m. This gradient amplitude can be achieved with custom built gradient coils [65].

The peak position $x_{b,\max}/\Delta x_p$ and the required length of the first gradient $t_{1,r} = 1000\Delta x_p^2/6/D$ are stated in Table I for these settings. The squid giant axon is not a feasible domain, since $t_{1,r}$ is too long, while $t_{1,r}$ of all other domains is in an experimentally accessible range. The thin axon is not a feasible domain either, since the edge enhancement cannot be suppressed to a reasonable degree, even if 50 T/m gradients are used. However, experiments on cells of 10 μm diameter seem to be feasible using one of the two larger gradient amplitudes with NAA as the diffusing particle. The alveoli of 200 μm diameter are accessible with the 50 T/m gradients, but the 1 T/m gradients, which are available for small animal scanners, result in severe edge enhancement artifacts.

B. Field inhomogeneities

1. *First gradient*

Magnetic resonance imaging and NMR diffusion experiments require a very homogeneous main magnetic field. Field inhomogeneities can lead to image artifacts and incorrectly measured diffusion values [11].

When performing diffusion pore imaging using temporally asymmetric gradients, the intention of the first gradient is to imprint a phase that is identical to the phase that the particle would acquire if it was located at the center of mass of the domain [see Eqs. (14) and (15)]. Assuming that there is—in addition to the gradient field—a susceptibility induced additional magnetic field $\Delta B_0(\mathbf{r})$, then the particle obtains the additional phase $\bar{\varphi}_+ = \gamma t_1 \overline{\Delta B_0}$ during the first gradient, where $\overline{\Delta B_0} = V^{-1}\int_\Omega \Delta B_0(\mathbf{r})d\mathbf{r}$ is the mean of the magnetic field inhomogeneity $\Delta B_0(\mathbf{r})$ in the pore. In other words: The particle was at every position with equal probability and thus acquires the phase corresponding to the mean magnetic field.

If all pores have identical $\Delta B_0(\mathbf{r})$, then only a net phase shift occurs. If different pores have different $\Delta B_0(\mathbf{r})$, then the overall signal is the sum of the complex signals of all pores, such that a signal void can occur (this is an interpore effect). For example, if $\overline{\Delta B_0}$ of the pores is distributed according to a Gaussian distribution of variance $\sigma^2_{\overline{\Delta B_0}}$, the overall signal decays according to $\exp(-\langle\bar{\varphi}_+^2\rangle/2) = \exp(-\gamma^2 t_1^2 \sigma^2_{\overline{\Delta B_0}}/2)$. Here, the expectation value brackets are understood to reflect the averaging process over all pores, and not that of an individual pore. In order to suppress this effect, the aim must be to minimize $\bar{\varphi}_+$ by an appropriate sequence technique. A straightforward sequence technique is depicted in Fig. 2. This sequence is similar to a Carr-Purcell-Meiboom-Gill (CPMG) echo train, e.g., if $\Delta B_0(\mathbf{r})$ is constant within a pore, its effect is canceled.

Another possible effect is that the signal drops due to diffusion weighting effects of $\Delta B_0(\mathbf{r})$, which generate a phase dispersion, just as linear gradients do [see the text following Eq. (2)]. This signal attenuation is proportional to $\langle\varphi^2\rangle$ in the motional narrowing regime [see Eqs. (34) and (36)]. The signal drop occurs for each pore individually (it is a single pore effect), and thus the brackets denote the averaging over a single pore.

TABLE I. Feasibility of diffusion pore imaging regarding the effect of finite first and second gradient.[a]

	L of slab, corresponds to diameter (μm)	D (μm^2/ms)	γ (1/s/T)	G (T/m)	Position of edge enhancement peak in units of pixel sizes $x_{b,\max}/\Delta x_p$	Required duration $t_{2,r}$ of second gradient (ms)	Required duration $t_{1,r}$ to reduce the blurring width σ_x to the pixel size Δx_p (ms)
Cell, water	10	2	2.675×10^8	0.045	13.5 $^{(--)}$	261	83 $^{(++)}$
	10	2	2.675×10^8	1	2.9 $^{(-)}$	11.7	83 $^{(++)}$
	10	2	2.675×10^8	50	0.41 $^{(++)}$	0.235	83 $^{(++)}$
Thin axon, water	1	2	2.675×10^8	0.045	428 $^{(--)}$	2610	0.83 $^{(++)}$
	1	2	2.675×10^8	1	91 $^{(--)}$	117	0.83 $^{(++)}$
	1	2	2.675×10^8	50	13 $^{(--)}$	2.35	0.83 $^{(++)}$
Squid giant axon, water	500	2	2.675×10^8	0.045	0.04 $^{(++)}$	5.22	208000 $^{(-)}$
	500	2	2.675×10^8	1	0.01 $^{(++)}$	0.235	208000 $^{(-)}$
	500	2	2.675×10^8	50	0.00 $^{(++)}$	0.0047	208000 $^{(-)}$
Soma of neuron, NAA	10	0.68	2.675×10^8	0.045	7.9 $^{(--)}$	261	245$^{(+)}$
	10	0.68	2.675×10^8	1	1.67 $^{(+)}$	11.7	245$^{(+)}$
	10	0.68	2.675×10^8	50	0.24 $^{(++)}$	0.235	245$^{(+)}$
Alveolus, xenon gas	200	5710	-7.400×10^7	0.045	15.4 $^{(--)}$	47	12$^{(++)}$
	200	5710	-7.400×10^7	1	3.26 $^{(--)}$	2.12	12$^{(++)}$
	200	5710	-7.400×10^7	50	0.46 $^{(++)}$	0.042	12$^{(++)}$
Diseased alveolus,	1000	5710	-7.400×10^7	0.045	1.38 $^{(+)}$	9.42	292$^{(+)}$
xenon gas	1000	5710	-7.400×10^7	1	0.29 $^{(++)}$	0.42	292$^{(+)}$
	1000	5710	-7.400×10^7	50	0.04 $^{(++)}$	0.0085	292$^{(+)}$

[a]The slab domain was used to estimate these parameters, and a pixel size $\Delta x_p = L/10$ was assumed. The feasibility of configurations was classified from "very good" $(++)$ to "very bad" $(--)$. A finite second gradient causes an edge enhancement. When the peak of the edge enhancement is less than Δx_p apart from the boundary, the configuration was classified with $(++)$. A finite first gradient causes a blurring of the image. The rightmost column specifies the duration $t_{1,r}$ of the first gradient that is required to reduce the blurring width σ_x so that it is equal to Δx_p. The classification of $t_{1,r}$ was performed with respect to typical transversal relaxation times (which are roughly 100 ms for water/NAA and 1 s for xenon gas). The diffusion coefficient of NAA was set to the free diffusion coefficient value that Ellegood *et al.* [106] measured in aqueous solution, and the diffusion coefficient of gaseous xenon was set to the value stated by Mair *et al.* [107]. The diffusion coefficient $D = 2\ \mu$m^2/ms is approximately the diffusion coefficient of water at room temperature as reported by Mills [108], and it is also approximately equal to the diffusion coefficient measured in the spinal cord along the fiber direction by Ries *et al.* [109].

As an example, consider a spherical pore with a parabolic field inhomogeneity $\Delta B_0(\mathbf{r}) = \Delta B_{0,L} \frac{r^2}{L^2}$, where L is the radius of the sphere, $r = |\mathbf{r}|$ is the radial coordinate, and $\Delta B_{0,L}$ is the additional magnetic field at the boundary. Then it follows that

$$\begin{aligned} \overline{\Delta B_0} &= \frac{3}{4\pi L^3} \int_\Omega \Delta B_0(\mathbf{r}) d\mathbf{r} \\ &= \frac{3}{4\pi L^3} \frac{\Delta B_{0,L}}{L^2} 4\pi \int_0^L r^2 r^2 dr \\ \Rightarrow \bar{\varphi}_+ &= \frac{3}{5} \gamma t_1 \Delta B_{0,L}. \end{aligned} \tag{45}$$

The signal drop due to diffusion (single-pore effect) can be estimated by the same approach as in Sec. III: Since the diffusion process is assumed to be in the long time limit, the Gaussian phase approximation is valid, and a generalized version of Eqs. (35) and (36), which was stated by Grebenkov [Eq. (119) in Ref. [28]], can be used to estimate the signal attenuation in that regime, which is caused by the field inhomogeneity:

$$\exp\left(-\gamma^2 \Delta B_{0,L}^2 t_1 L^2 D^{-1} \tilde{\zeta}_{-1}\right). \tag{46}$$

Here, $\tilde{\zeta}_{-1}$ is again a geometry dependent constant, which is 8/2625 for parabolic gradient fields in spherical domains (see Table II in Ref. [28], p. 1102).

2. *Second gradient*

The second gradient is essentially an imaging gradient. The sampling of the q space is performed similarly as in single-point imaging [66,67], or in chemical shift imaging [4,68], but not as in conventional NMR imaging. In particular, no frequency encoding gradient is applied (in q space). In NMR imaging, if a field inhomogeneity is present, it generates a linear phase in k space, and thus an image distortion in image space. This effect is most pronounced when using long signal readouts, e.g., in echoplanar sequences [4,69]. However, these distortions are not present in the pore imaging technique, since the readout is performed after application of the gradient. As a consequence, a field inhomogeneity merely generates an additional phase in image space.

3. *Impact on experimental settings*

Susceptibility induced field inhomogeneities in biological tissue are usually small [70], except when many tissue-air interfaces are present, as in lung tissue. Relying on a foam model, Case *et al.* [71] found that the typical field shift inside a pore is about 5 ppm, which roughly corresponds to $\Delta B_{0,L} = 5\ \mu$T at 1 T field strength. Using Eqs. (45) and (46), and assuming the parameters $t_1 \approx T = 100$ ms, radius of sphere $L = 100\ \mu$m, $D = 5710\ \mu$m^2/ms (xenon gas), and $\gamma = -7.400 \times 10^7$ s^{-1} T^{-1} (^{129}Xe), one finds that the signal

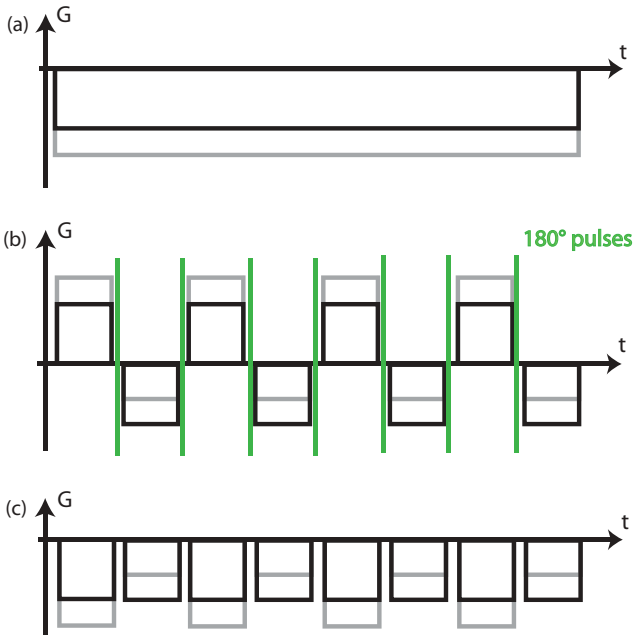

FIG. 2. (Color online) (a) First diffusion gradient (black) and the same diffusion gradient perturbed by a susceptibility induced gradient (gray). (b) Alternative gradient scheme with 180° pulses between the gradients. (c) Effective gradients of (b). The effect of the susceptibility induced gradient is minimized by the magnetization inversions.

drops to 92.9%, while $\bar{\varphi}_+$ is 22.23. If the field strength is 3 T, the signal drops to 51.7% and $\bar{\varphi}_+$ is 66.69.

Thus, the signal drop is not a major problem for these parameters, but it should be kept in mind that Eq. (46) predicts an exponential signal drop, and the argument of the exponential function is proportional to squared length and proportional to the square of $\Delta B_{0,L}$, so that larger domains or higher field strengths can easily result in a vanishing signal. The phase $\bar{\varphi}_+$ is large, but it can be compensated by spin echoes (or trains of spin echoes as in Fig. 2), so that this phase issue should not be a major problem in an experimental setting.

C. Surface relaxation

Whereas surface relaxation can usually be neglected in biological tissue, it is of great importance in nonbiological porous media [72,73]. There are basically two problems that can arise when performing pore imaging when surface relaxation is present. The final particle distribution may not be homogeneous as assumed in Eq. (14), and the first gradient may not yield the phase corresponding to the center of mass $\mathbf{x}_{\text{c.m.}}$ of the domain.

1. Inhomogeneous magnetization

If surface relaxation is present, the magnetization becomes nonuniform, and the integral $\int_\Omega d\mathbf{x}\exp(i\,\mathbf{q}\cdot\mathbf{x})$ of Eq. (14) must be converted to $\int_\Omega d\mathbf{x}\,V\mathfrak{m}(\mathbf{x},t)\exp(i\,\mathbf{q}\cdot\mathbf{x})$. Note that $V\mathfrak{m}(\mathbf{x},t)$ is dimensionless. As in Eq. (20), $\mathfrak{m}(\mathbf{x},t)$ at time $t=0$ can be formally expanded in eigenfunctions of the Laplace operator $\mathfrak{m}(\mathbf{x},t=0)=V^{-1/2}\sum_{m=0}^{\infty}U_m u_m(\mathbf{x})$. As time evolves, the contribution of the eigenfunctions decreases according to the diffusion equation as $u_m(\mathbf{x})e^{-Dt\lambda_m/L^2}$, where λ_m is the eigenvalue corresponding to the eigenfunction $u_m(\mathbf{x})$. In the long time limit in single length scale domains, only the smallest eigenfunction $u_0(\mathbf{x})$ survives. Thus, we expect $\mathfrak{m}(\mathbf{x},t\to\infty)\propto u_0(\mathbf{x})$. This is reasonable from a physical point of view, since eigenfunctions corresponding to larger eigenvalues represent higher spatial frequencies which are smeared out by the diffusion process.

For example, the eigenfunctions of a slab of unit length with surface relaxivity ρ and with the dimensionless surface relaxivity parameter $h=\rho L/D$ are

$$u_m(x)=\sqrt{2\lambda_m}\left(\lambda_m+2h+h^2\right)^{-1/2}\times\left(\cos(\alpha_m x)+\frac{h}{\alpha_m}\sin(\alpha_m x)\right), \tag{47}$$

where $\alpha_m=\sqrt{\lambda_m}$ are the kernels of the equation

$$\frac{\tan(\alpha_m)}{\alpha_m}=\frac{2h}{\alpha_m^2-h^2}. \tag{48}$$

For initially homogeneous magnetization, the coefficients U_m are (see Ref. [28])

$$U_m=\sqrt{2}h(1+(-1)^m)\lambda_m^{-1/2}(\lambda_m+2h+h^2)^{-1/2}. \tag{49}$$

Thus we expect for the magnetization

$$\mathfrak{m}(x,t\to\infty)\propto\sqrt{2\lambda_0}(\lambda_0+2h+h^2)^{-1/2}\times\left(\cos(\alpha_0 x)+\frac{h}{\alpha_0}\sin(\alpha_0 x)\right). \tag{50}$$

For example, the surface relaxation ρ in sandstone was determined by Hürlimann *et al.* [74] to be 16 μm/s with a surface to volume ratio of $(7\ \mu\text{m})^{-1}$. This results in a rather small $h\approx 0.1$ assuming $L=7\ \mu$m and $D=1\ \mu\text{m}^2/\text{ms}$.

2. Apparent shrinkage and shift of the pore image

Due to the diffusive motion, the signal decays as

$$\mathfrak{m}(\mathbf{x},t\to\infty)\propto u_0(\mathbf{x})e^{-Dt\lambda_0/L^2}. \tag{51}$$

The zeroth eigenvalue λ_0 can be found for single length scale domains by solving equations similar to Eq. (48) [28]. If we assume small surface relaxivities, λ_0 can usually be expanded in $h=\rho L/D$. For example, one finds for the slab domain

$$\lambda_0=2h-\tfrac{1}{3}h^2+O(h^2), \tag{52}$$

and thus to leading order in h,

$$\mathfrak{m}(\mathbf{x},t\to\infty)\propto u_0(\mathbf{x})e^{-2\rho T/L}. \tag{53}$$

Imagine a domain with two characteristic length scales L_1 and L_2 as depicted in Fig. 3. The magnetization in the region of short characteristic length scale L_1 decays at large t, since particles are more likely to be "eaten" at the boundary. This causes a signal void, the information on the small structures is lost, and only the magnetization in the bulk survives. Consequently, the measured pore shrinks and the center of mass $\mathbf{x}_{\text{c.m.},1}$ [Eq. (9)] at large t shifts from $\mathbf{x}_{\text{c.m.},1}$ to some other position $\mathbf{x}_{\text{c.m.},1,h>0}$, thus resulting in a shift of the pore image.

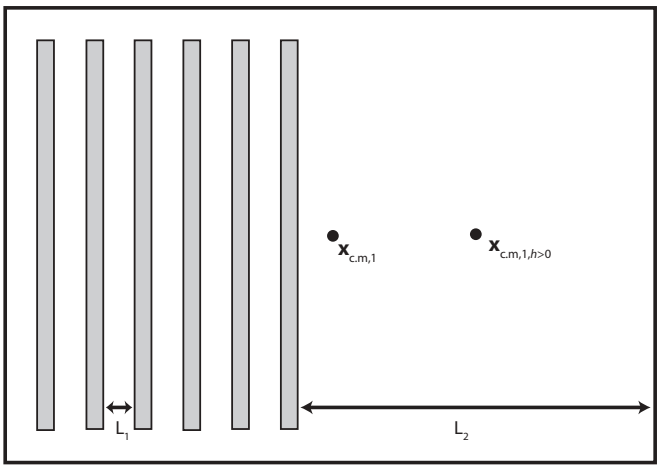

FIG. 3. Shift of the center of mass of the particle trajectory by surface relaxation $h > 0$ from $\mathbf{x}_{\text{c.m.},1}$ to another position $\mathbf{x}_{\text{c.m.},1,h>0}$. A two-length scale domain is plotted. Surface relaxation occurs at the outer rectangular boundary and at the boundary of the grey boxes. At long times, the signal has mostly decayed in the left half, while it partly survives in the right half of the domain. Consequently the pore shrinks and the center of mass of the particle trajectory is shifted to the center of the right half of the domain. The resulting diffusion pore image is shifted accordingly.

V. IMAGINARY PART OF THE SIGNAL ATTENUATION AND SYMMETRY OF THE DOMAIN

As stated by Bergmann and Dunn [44] and Grebenkov [28], the imaginary part of the signal attenuation $\text{Im}(S)$ vanishes if the temporal profile of the diffusion weighting gradients is antisymmetric as $\mathbf{G}(t) = -\mathbf{G}(T-t)$. This statement can be justified by considering an arbitrary path $\mathbf{x}(t)$ and the corresponding reverse path $\mathbf{y}(t) = \mathbf{x}(T-t)$. These two paths are visualized for a discrete 4-step random walk in an equilateral triangular domain in Figs. 4(a) and 4(b). A particle following the path $\mathbf{x}(t)$ obtains the phase

$$\varphi_{\text{path1}} = \gamma \int_0^T \mathbf{G}(t) \cdot \mathbf{x}(t) dt. \tag{54}$$

A particle following the reverse path obtains the phase

$$\varphi_{\text{path2}} = \gamma \int_0^T \mathbf{G}(t) \cdot \mathbf{y}(t) dt = \gamma \int_0^T \mathbf{G}(t) \cdot \mathbf{x}(T-t) dt. \tag{55}$$

Introducing the variable $t' = T - t$, this expression becomes

$$\begin{aligned} \varphi_{\text{path2}} &= -\gamma \int_T^0 \mathbf{G}(T-t') \cdot \mathbf{x}(t') dt' \\ &= \gamma \int_0^T \mathbf{G}(T-t') \cdot \mathbf{x}(t') dt', \end{aligned} \tag{56}$$

and hence

$$\varphi_{\text{path2}} = -\gamma \int_0^T \mathbf{G}(t') \cdot \mathbf{x}(t') dt' = -\varphi_{\text{path1}}. \tag{57}$$

As each path has its reverse path, the expectation values of the odd moments $(\langle\varphi\rangle, \langle\varphi^3\rangle \langle\varphi^5\rangle, \ldots)$ vanish, since the contributions of path and reverse path cancel. For example, $\varphi^3_{\text{path1}} + \varphi^3_{\text{path2}} = 0$. The even moments do not vanish, e.g., $\varphi^2_{\text{path1}} + \varphi^2_{\text{path2}} \neq 0$. The signal attenuation $S = \langle \exp(-i\varphi) \rangle$ can be expanded in its moments:

$$S = 1 - i\langle\varphi\rangle - \tfrac{1}{2}\langle\varphi^2\rangle + \tfrac{1}{6} i \langle\varphi^3\rangle + \tfrac{1}{24}\langle\varphi^4\rangle + \cdots. \tag{58}$$

As the odd moments vanish for temporally antisymmetric gradients, it follows that S is real.

If the temporal gradient profile is not antisymmetric, the above reasoning, and in particular the step from Eqs. (56)

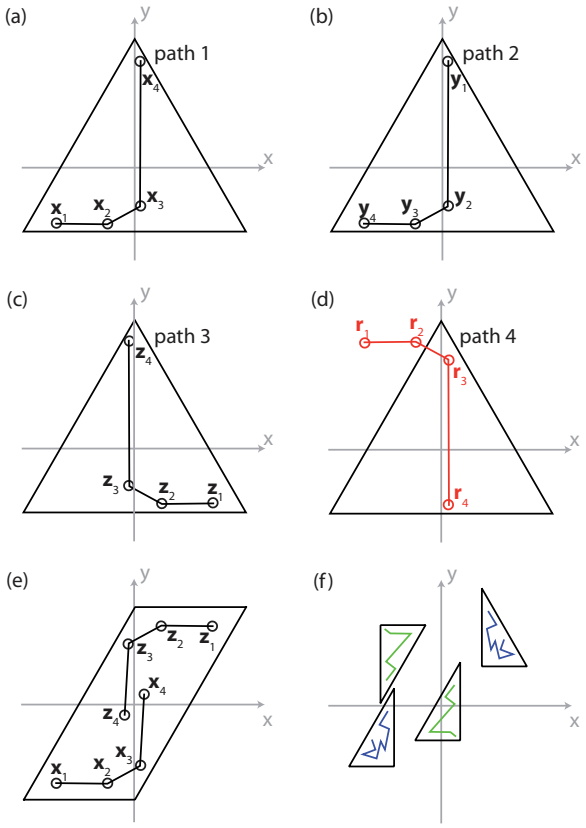

FIG. 4. (Color online) Imaginary signal attenuation $\text{Im}(S)$ and its relation to symmetries of the domain. (a) A discrete 4-step random walk in an equilateral triangular domain. The particle following this path $\mathbf{x}(t)$ obtains a certain phase φ_{path1}. (b) Another particle follows the reverse path $\mathbf{y}(t)$ and obtains the phase φ_{path2}. If the temporal gradient profile is antisymmetric as $\mathbf{G}(t) = -\mathbf{G}(T-t)$, it holds true that $\varphi_{\text{path2}} = -\varphi_{\text{path1}}$ in any domain. This leads to the cancellation of odd moments $\langle\varphi^{2n+1}\rangle$, and consequently the imaginary signal attenuation $\text{Im}(S)$ must be zero. (c) Using temporally nonantisymmetric gradients, $\text{Im}(S)$ is in general unequal to zero. However, if a mirror symmetry is present (gradient along the x direction), the mirrored path $\mathbf{z}(t)$ can cancel the contribution of the original path $\mathbf{x}(t)$ and $\text{Im}(S)$ is zero, even if $\mathbf{G}(t) \neq -\mathbf{G}(T-t)$. (d) If the gradient is applied along the y direction, the mirrored path $\mathbf{r}(t)$ does not exist, and $\text{Im}(S)$ can deviate from zero. (e) Besides mirror symmetries, symmetry under parity does also enforce $\text{Im}(S) = 0$, even if $\mathbf{G}(t) \neq -\mathbf{G}(T-t)$. (f) Assuming a gradient in the x direction: Even asymmetric domains (or domain distributions) can yield $\text{Im}(S) = 0$ if exactly one path of opposite phase can be mapped one to one to every possible path.

to (57), is not possible. Nonetheless, it turns out that a similar analysis can be performed if the domain is mirror symmetric with respect to a plane perpendicular to the gradient direction. Assume, for example, that the equilateral triangular domain depicted in Fig. 4(a) is measured with a gradient in the x direction: $\mathbf{G}(t) = [G_1(t),0,0]^T$. Instead of considering the reverse path, we now consider the mirrored path $\mathbf{z}(t)$, which is identical to the path $\mathbf{x}(t) = [x_1(t),x_2(t),x_3(t)]^T$ mirrored with respect to the y-z plane. Hence, $\mathbf{z}(t) = [z_1(t),z_2(t),z_3(t)]^T = [-x_1(t),x_2(t),x_3(t)]^T$.

Under these assumptions, the phases that particles obtain following path $\mathbf{x}(t)$ or $\mathbf{z}(t)$, respectively, are

$$\varphi_{\text{path}1} = \gamma \int_0^T \mathbf{G}(t)\cdot\mathbf{x}(t)dt = \gamma \int_0^T G_1(t)\cdot x_1(t)dt, \quad (59)$$

$$\varphi_{\text{path }3} = \gamma \int_0^T \mathbf{G}(t)\cdot\mathbf{z}(t)dt = \gamma \int_0^T G_1(t)\cdot z_1(t)dt$$
$$= -\gamma \int_0^T G_1(t)x_1(t)dt. \quad (60)$$

Thus, path and mirrored path cancel when computing the odd moments of φ, and $\mathrm{Im}(S)$ is zero.

If no mirror symmetry is present, it is not always possible to find a second path of opposite phase. For example, there exists no path $\mathbf{r}(t)$ that corresponds to path 1 mirrored with respect to the x-z plane as depicted in Fig. 4(d). Consequently, $\mathrm{Im}(S)$ can in general be unequal zero as described in Sec. II.

Other symmetry properties of the domain can also enforce a vanishing imaginary signal. For example, the parallelogram depicted in Fig. 4(e) is symmetric under parity transformation. It yields a vanishing imaginary signal if the gradient is aligned along the x axis since a point-reflected path $\mathbf{z}(t)$ of opposite phase can be found for every path $\mathbf{x}(t)$. Eventually the vanishing of $\mathrm{Im}(S)$ is enforced by the existence of exactly one path of opposite phase for each possible path. For example, the four triangular domains depicted in Fig. 4(f) are not aligned in a particular symmetric fashion, but it is possible to find paths of opposite phase (marked in green/light gray and blue/dark gray), and hence $\mathrm{Im}(S) = 0$ for a gradient in the x direction.

We now consider the question of how the signal transforms under mirror reflection of the domain. Again, the reflection plane (e.g., y-z) is assumed to be perpendicular to the gradient direction (e.g., x). If the domain is mirror reflected, the path $\mathbf{x}(t)$ is transformed into the reflected path $\mathbf{z}(t)$. Thus, the phase that a particle obtains following this path changes sign ($\varphi_{\text{path }1} = -\varphi_{\text{path }3}$). Consequently, even moments are invariant under mirror reflections, while the sign of odd moments flips:

$$\langle\varphi^{2n}\rangle \xrightarrow{\text{reflection}} \langle\varphi^{2n}\rangle, \quad (61)$$

$$\langle\varphi^{2n+1}\rangle \xrightarrow{\text{reflection}} \langle-\varphi^{2n+1}\rangle. \quad (62)$$

Here, n is a natural number. It follows for the signal attenuation that

$$S \xrightarrow{\text{reflection}} S^*. \quad (63)$$

Temporally antisymmetric and nonantisymmetric gradients differ in their ability to distinguish reflected and original domains. For example, the domain configuration depicted in

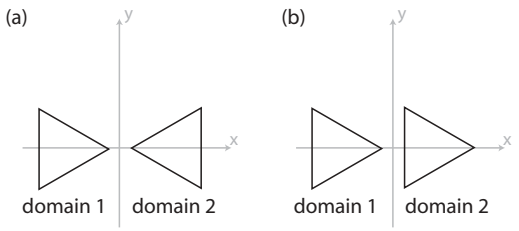

FIG. 5. Spatial coherence becomes detectable using temporally nonantisymmetric diffusion gradients. Using temporally antisymmetric gradients $\mathbf{G}(t) = -\mathbf{G}(T-t)$, the two triangular domains of opposite orientation depicted in (a) yield the same signal as those depicted in (b). The gradient direction is assumed to be along the x direction. Using nonantisymmetric gradients $\mathbf{G}(t) \neq -\mathbf{G}(T-t)$, the signal intensity of the domains depicted in (a) is smaller than that of the domains depicted in (b): Spatial coherence becomes detectable in the signal intensity, without the need to measure imaginary signal attenuation directly.

Fig. 5(a) yields the signal

$$S = S_{\text{domain }1} + S_{\text{domain }2} = S_{\text{domain }1} + S^*_{\text{domain }1} = 2\mathrm{Re}(S_{\text{domain }1}) \quad (64)$$

if the gradient is applied along the x direction. Using temporally antisymmetric gradients, one finds the following relation to the absolute value of the signal attenuation (later we also label $|S|$ as signal intensity):

$$|S| = \sqrt{S\cdot S^*} = 2|S_{\text{domain1,antisym}}|. \quad (65)$$

However, using nonantisymmetric gradients, the occurring imaginary parts cancel such that

$$|S| \leqslant 2|S_{\text{domain1,nonantisym}}| \quad (66)$$

holds true. In practice, this might allow to infer information about the relative spatial orientation of pores: The signal of coherently oriented pore [Fig. 5(b)] is larger than that of incoherently oriented pores [Fig. 5(a)] when using nonantisymmetric gradients.

Antisymmetric and nonantisymmetric gradients have also different properties regarding the real signal attenuation $\mathrm{Re}(S)$. For example, using q-space gradients, the signal in the motional narrowing regime of closed domains is strictly positive [see Eq. (13)]. Although we are not aware of a general proof, this seems to be a universal feature of antisymmetric gradients. In contrast, nonantisymmetric gradients can yield negative $\mathrm{Re}(S)$, even if $\mathrm{Im}(S) = 0$. For example, performing diffusion pore imaging of a slab domain yields a sinc-shaped profile of S, which contains negative values.

We conclude this section with a comment about the position of the mirror plane. The diffusion gradients are supposed to fulfill the rephasing condition $\int_0^T \mathbf{G}(t)dt = 0$. Hence, the phase is invariant under translation by $\Delta\mathbf{x}_{\text{plane}}$:

$$\varphi_{\text{translated}} = \gamma \int_0^T \mathbf{G}(t)\cdot[\mathbf{x}(t) + \Delta\mathbf{x}_{\text{plane}}]dt$$
$$= \gamma \int_0^T \mathbf{G}(t)\cdot\mathbf{x}(t)dt + \gamma\Delta\mathbf{x}_{\text{plane}}\cdot\int_0^T \mathbf{G}(t)dt$$
$$= \varphi_{\text{untranslated}} + 0. \quad (67)$$

Thus, the mirror plane can be located at any position.

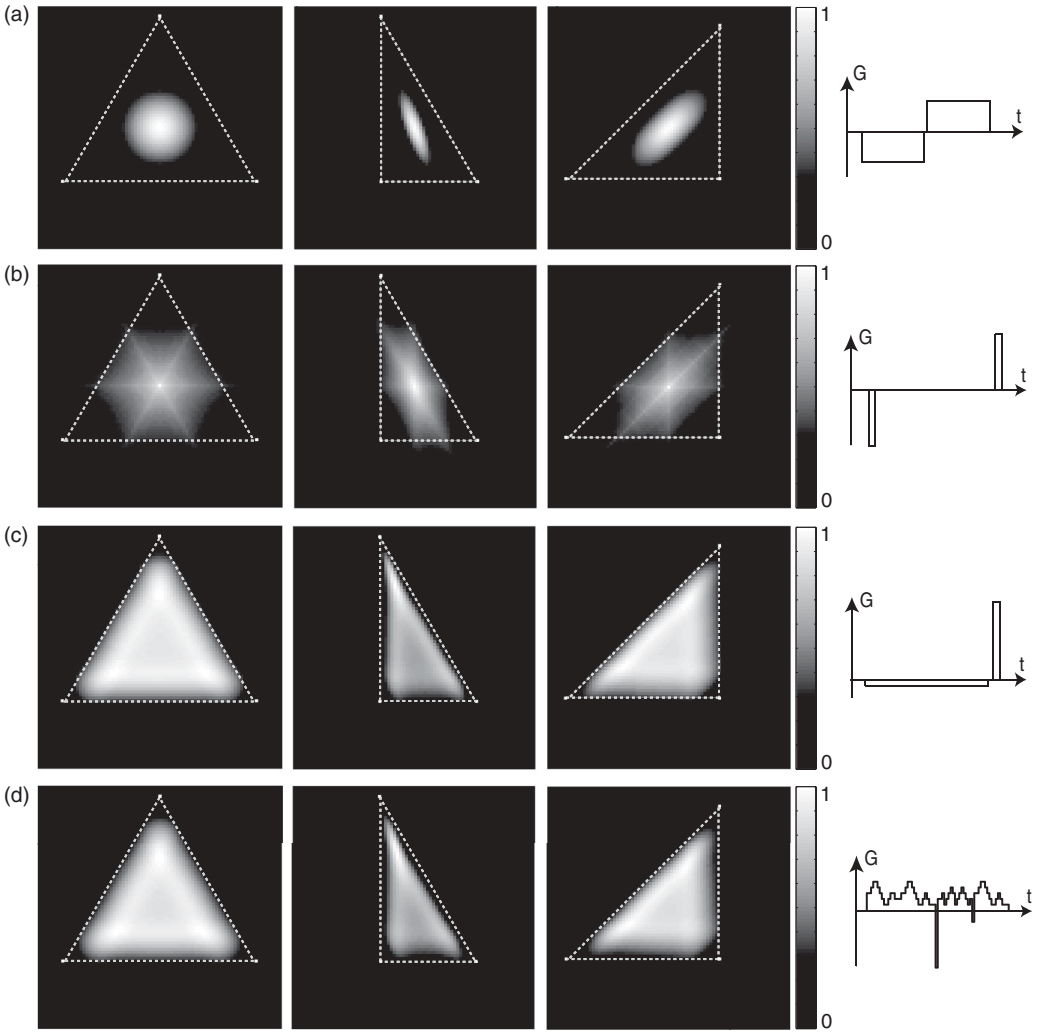

FIG. 6. Diffusion pore imaging of three triangular domains using antisymmetric (a), q-space imaging (b), the original pore imaging gradient profile (c), and the gradient profile $f_{\text{An Die Freude}}$ (d). The images were obtained by performing a Fourier transformation of the q-space data. The signal in (a) is shaped as a Gaussian function, reflecting the validity of the Gaussian phase approximation. Using q-space gradients (b), the triangular shape cannot be estimated by the obtained signal pattern. In particular, since the phase information is lost, the signal is point symmetric (unlike the domain). The triangular boundaries can clearly be appreciated in (c) and in (d). Parameters: $D = 1\ \mu\text{m}^2/\text{ms}$, $L = 10\ \mu\text{m}$, $T = 100$ ms, number of used eigenvalues is 40, and a 81×81 matrix of q space was sampled in steps of $0.5\ \mu\text{m}^{-1}$ (equilateral and hemiequilateral triangle) and $0.4\ \mu\text{m}^{-1}$ (isosceles triangle). (a) $t_1 = 50$ ms, $t_2 = 50$ ms. (b) $t_1 = 1$ ms, $t_2 = 1$ ms. (c) $t_1 = 99$ ms, $t_2 = 1$ ms.

VI. SIMULATIONS

A. Pore imaging

Figure 6 shows the Fourier transform of the signal attenuation $S(\mathbf{q})$ [see Eq. (14)] for three triangular model domains (dotted lines). Stejskal-Tanner gradients were used in Fig. 6(a), q-space imaging gradients were used in Fig. 6(b), and temporally asymmetric gradients were used in Figs. 6(c) and 6(d). In Fig. 6(a), the signal is approximately shaped as a Gaussian function, and the shape of the domain is not well reflected in the signal. This is a consequence of the Gaussian phase approximation, which is valid in the motional narrowing regime if long diffusion gradients are used: Since $S(\mathbf{q})$ is a Gaussian function, the Fourier transform depicted in Fig. 6(a) is also a Gaussian function. In Fig. 6(b), the phase information is lost, and the triangular structure cannot be resolved. In particular, due to the lost phase information, $S(\mathbf{q})$ and $S(-\mathbf{q})$ are identical and the signal in Fig. 6(b) has a hexagonal rather than a triangular shape. In contrast, by using asymmetric gradients [Fig. 6(c)], the structure of the domain can be assessed, since the phase information is preserved. The edge enhancement and the signal drop at the boundary are clearly visible (see Sec. IV A2). Figure 6(d) demonstrates that diffusion pore imaging can be performed using a much wider class of gradient profiles than the originally proposed profile [Eqs. (6) and (32)].

B. Gradient duration

Figures 7(a) and 7(b) show the COM distribution of $\mathbf{x}_{\text{c.m.},1}$ for the equilateral triangle using a constant first gradient [Fig. 7(a)] and for the profile $f_{\text{An Die Freude}}$ (without the sharp gradient pulse). Values simulated using the MCF technique (dots, see Sec. III) correspond well to the theoretical

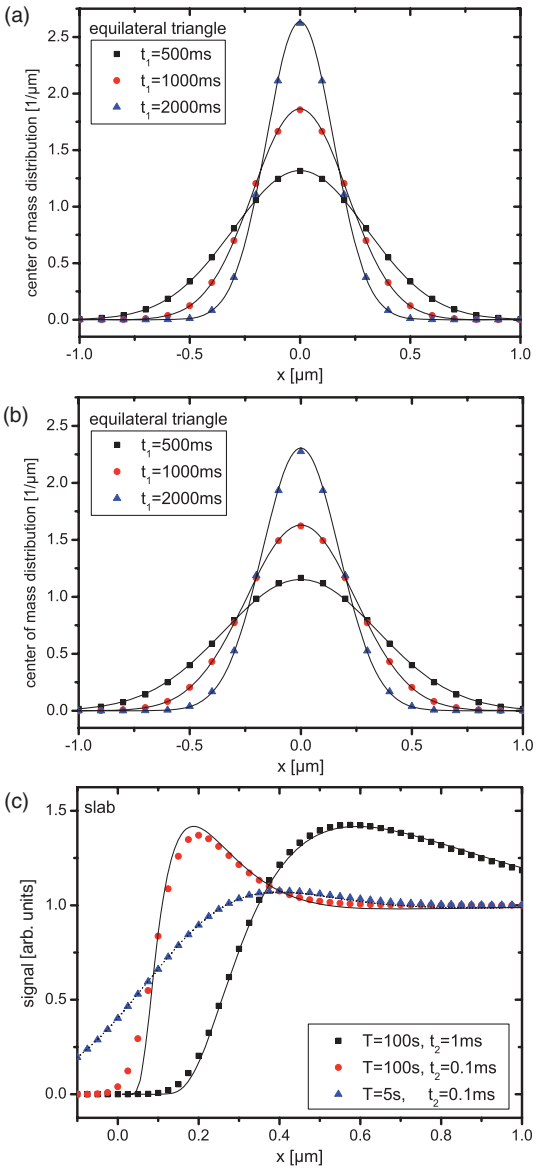

FIG. 7. (Color online) Effect of infinite first gradient and noninfinitesimal second gradient. (a) Constant first gradient. (b) "An die Freude" gradient profile [Eq. (33)] without a sharp gradient pulse. In (a) and (b), the distribution of the center of mass of the trajectory that a particle follows during the first gradient is described by a Gaussian function that becomes smaller at large t_1 and converges towards the Dirac delta function for $t_1 \to \infty$. Simulated values (squares, circles, triangles) and the theoretical expression [solid line, Eq. (41)] are in good agreement. Owing to the larger I_f value [see Eqs. (35)–(38)], the width of the Gaussian function is larger in (b) than in (a). (c) Second gradient not infinitesimal: An edge enhancement effect occurs (squares, circles) and the peak of the signal is pushed away from the boundary at $x = 0$ μm. Simulated values (squares, circles) are in good agreement with the edge enhancement curve [Eq. (42), solid lines], although a residual blurring due to the noninfinite first gradient is observable. Simulations show that the blurring becomes more prominent when t_1 is reduced (triangles). The blurring is well described by a convolution of the nonblurred edge enhancement curve [Eq. (42), solid line] with the center of mass distribution [Eq. (41), see (a) and (b)]: The convolved function is represented by the dotted line. Simulation parameters: $t_1 + t_2 = T$, number of used eigenvalues is 50, $D = 1$ μm^2/ms, slab distance $L = 10$ μm.

expressions given by Eqs. (40) and (41) (solid lines). The simulated values of the COM distribution were obtained by Fourier transformation of the signal attenuation

$$S(q_G) = [\exp[-(p\Lambda - iq_G\mathcal{B})t_1/T]]_{0,0}. \tag{68}$$

Figure 7(c) shows the edge enhancement effect for the slab domain. Simulated values are plotted as dots (squares, circles, triangles). The slab domain was chosen since this allows the comparison to Mitra and Halperin's theoretical edge enhancement expression [Eq. (42), see Ref. [38]]. The solid line represents Eq. (42) and is in good agreement with simulations if the first gradient is sufficiently long ($t_1 \approx 100$ s, red circles and black squares). Only a small residual blurring is observable. However, if the first gradient is not sufficiently long ($t_1 \approx 5$ s), a prominent blurring occurs (blue triangles). The dotted line represents the convolution of the edge enhancement line [Eq. (42), solid line in Fig. 7(c)] and the COM distribution of $\mathbf{x}_{\mathrm{c.m.},1}$ [Eq. (41)], and is in good agreement with the simulated values (blue triangles).

In practice, these two effects—edge enhancement and blurring—compete, and both determine the resulting signal profile. The edge enhancement peak becomes broader with increasing t_2, while the blurring becomes stronger at shorter t_1. Thus, the ability of the blurring to smear out the peak depends on t_1 and t_2. Moreover, when the distance of the edge enhancement peak from the boundary becomes as large as the size of the domain, the peaks of different boundaries start to overlap.

C. Field inhomogeneities

To estimate the effect of local field inhomogeneities, a spherical pore with parabolic field inhomogeneity was chosen, since Grebenkov published the necessary matrices for parabolic fields (see Table I in Ref. [28]). The parabolic field can be used as a model for an occurring inhomogeneity of the main magnetic field.

Three situations were considered: (1) No parabolic field is present [$\Delta B_{0,L} = 0$ μT, Figs. 8(a) and 8(b)]. (2) A small parabolic field is present [$\Delta B_{0,L} = 5$ μT, Figs. 8(c)–8(f)]. (3) A large parabolic field is present ($\Delta B_{0,L} = 15$ μT, Fig. 9). Simulations were performed for the two gradient schemes displayed in Figs. 2(a) and 2(b).

Figures 8 and 9 show that the magnitude image is almost unperturbed by the additional parabolic gradient. Owing to the field inhomogeneity, a certain signal drop, which is caused by the occurring diffusion weighting effect, is observable: The signal in the pore center in Figs. 8(c) and 9(a) is only 93.0% and 51.8%, respectively, in comparison to the signal in the center of in Fig. 8(a). This is in good agreement with the factors 92.9% and 51.7% that are predicted by Eq. (46). It is further observable that the field inhomogeneity results in a phase shift. The phase shift in the center of the pore is $-2.94 \hat{=} 8\pi - 2.94 = 22.19$ for $\Delta B_{0,L} = 5$ μT and $-2.52 \hat{=} 22\pi - 2.52 = 66.17$ for $\Delta B_{0,L} = 15$ μT [Figs. 8(d) and 9(b)]. Both values are in good agreement with Eq. (45), which predicts phase shifts of 22.23 and 66.69, respectively. The spin echo compensation technique using multiple 180° radio frequency (rf) pulses as proposed in Fig. 2(b) yields a good suppression of the phase shift [Figs. 8(f) and 9(d)], but only

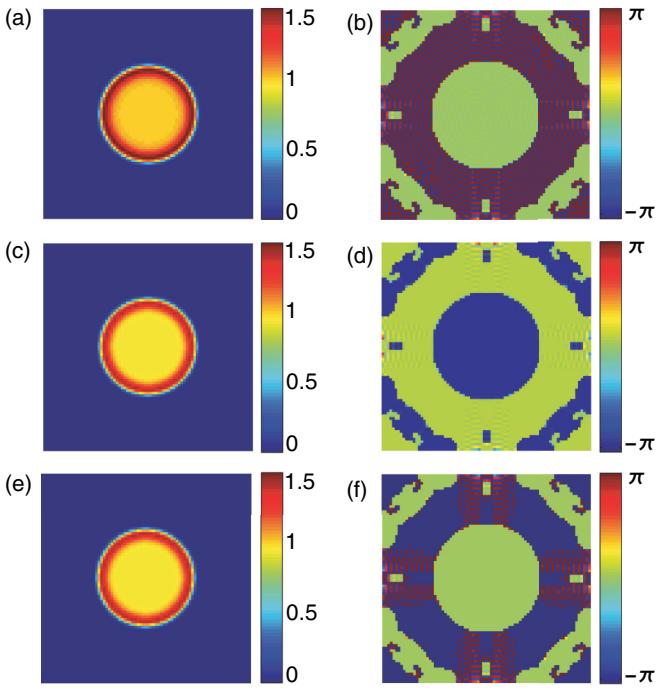

FIG. 8. (Color) Effect of field inhomogeneities on diffusion pore imaging of a spherical pore with a parabolic field inhomogeneity. Left column: Magnitude images. Right column: Phase images in radians. (a), (b) No inhomogeneity. (c), (d) Parabolic inhomogeneity of 5 μT and linear gradients as in Fig. 2(a). (e), (f) Parabolic inhomogeneity of 5 μT and linear gradients as in Fig. 2(b), seven inversions. The magnitude images are almost unperturbed by the field inhomogeneity, but a phase shift can be observed in (d). (f) shows that this phase shift can be suppressed by applying refocusing pulses. The edge enhancement effect is visible in the magnitude images. Magnitude images were scaled such that the pore center of (a) is equal to 1. Parameters: Radius $L = 100$ μm, $D = 5710$ μm^2/ms, $T = 100$ ms, $t_1 = 99.9$ ms, $t_2 = 0.1$ ms, and the number of used eigenvalues is 60. A 81×81 matrix of q space was sampled in steps of $0.005\ \pi\ \mu$m^{-1}.

results in a minor decrease of the diffusion weighting effect. The latter is in accordance with Eq. (35): When the motional narrowing approximation is valid, 180° rf pulses do not change the signal attenuation. A 180° rf pulse changes the sign of $f(\tau)$, e.g., from $f(\tau) = 1$ to $f(\tau) = -1$, which does not change the squared function $f^2(\tau)$ present in the integrand of Eq. (35). This is a property that is completely different in the short time limit (see, e.g., Refs. [28,30]). If many more inversion pulses are applied, one reaches the short time limit and the signal drop can be reduced. However, for the parameters used in Fig. 9, 99 inversions are not sufficient as the signal still drops to 57.8%. Using 999 inversions, the signal drops to 92.7%. This, however, would require applying an inversion pulse every 0.1 ms.

D. Surface relaxation

Figure 10 shows the signal profile of a pore image of a slab domain with zero and nonzero surface relaxivity $h \geqslant 0$. Simulated values (dots) and the corresponding, rescaled zeroth eigenfunction $u_0(\mathbf{x})$ (solid line) are in good agreement [see Sec. IV C 1 and Eq. (50)]. Due to surface relaxation, the signal

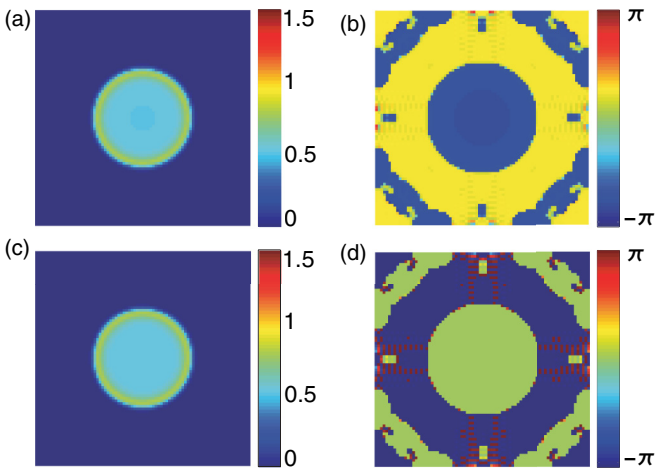

FIG. 9. (Color) Effect of field inhomogeneities on diffusion pore imaging of a spherical pore with a parabolic inhomogeneity of 15 μT. Left column: Magnitude images. Right column: Phase images in radians. (a), (b) Linear gradients as in Fig. 2(a). (c), (d) Linear gradients as in Fig. 2(b), seven inversions. The magnitude images are almost unperturbed by the field inhomogeneity, but a signal drop due to a diffusion weighting effect of the parabolic field is observable: The signal intensity is decreased when compared to Figs. 8(a) and 8(c). Using inversion pulses, the phase shift can still be suppressed (d). Magnitude images were scaled such that the pore center of Fig. 8(a) is equal to 1. Parameters: Radius $L = 100$ μm, $D = 5710$ μm^2/ms, $T = 100$ ms, $t_1 = 99.9$ ms, $t_2 = 0.1$ ms, and the number of used eigenvalues is 60. A 81×81 matrix of q space was sampled in steps of $0.005\ \pi\ \mu$m^{-1}.

intensity decreases near the boundary ($h = 1$, 5 and 10). This signal drop is more pronounced at larger surface relaxivities. The signal in the center of the slab is higher at larger surface relaxivities since it was normalized [see Eq. (28)].

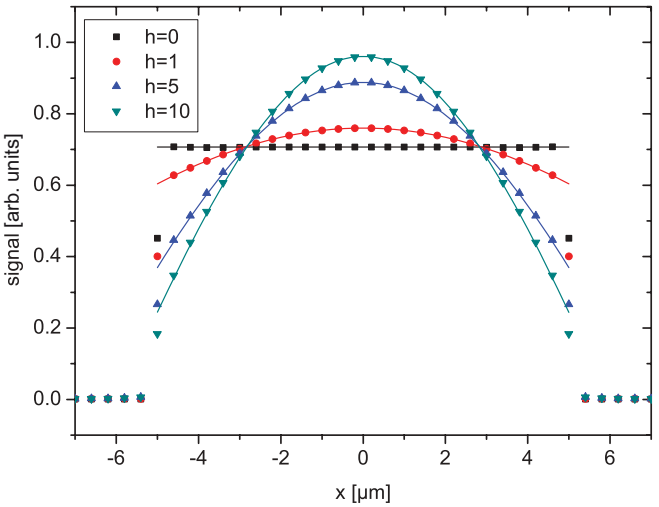

FIG. 10. (Color online) Diffusion pore image of a slab domain with surface relaxation $h = \rho L/D > 0$. Simulated values (dots) are well described by the zeroth eigenfunction $u_0(\mathbf{x})$ (solid line). Parameters: $T = 10$ s, $t_1 + t_2 = T$, $t_2 = 0.01$, $D = 1$ μm^2/ms, $L = 10$ μm, and the number of used eigenvalues is 40.

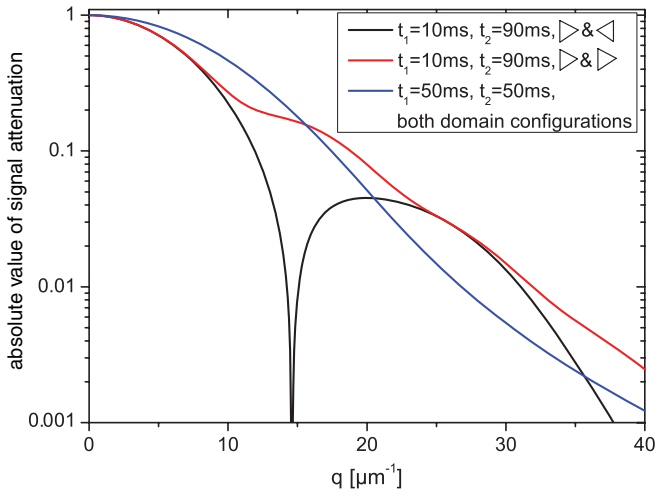

FIG. 11. (Color) Temporally asymmetric diffusion gradient profiles potentially reveal microscopic incoherent domain ordering. Two domain configurations are considered: two coherently and two incoherently ordered equilateral triangles (see Fig. 5). If the temporal gradient profile is antisymmetric (blue line), both configurations yield the same signal intensity. If the temporal gradient profile is nonantisymmetric (black and red line), the two configurations yield different signal intensities. If both triangles are ordered coherently, their signal adds up (red line). If they are ordered incoherently, the imaginary signal of the two domains cancel in this example, and the absolute value of the signal attenuation decreases (black line). Thus it is possible to distinguish these two configurations. The requirements on the asymmetry are quite moderate in this example ($t_2/t_1 = 9$). Parameters: $T = 100$ ms, $t_1 + t_2 = T$, $D = 1\ \mu\text{m}^2/\text{ms}$, $L = 10\ \mu$m, the number of used eigenvalues is 40, and the gradient along the x direction is as in Fig. 5.

E. Diffusion weighted phase

Figure 11 shows that temporally asymmetric gradient profiles can distinguish different relative orientations of two simultaneously measured domains. Simulations were performed for the domain configuration depicted in Fig. 5. The signal of the two triangles of equal orientation adds up (red/light gray line), while the imaginary signal of the two triangles of opposite orientation cancel. Consequently, also the absolute value of the signal intensity [Eq. (65)] drops (black line). Antisymmetric diffusion gradients yield the same signal intensity, independently of the relative domain orientation (blue/dark gray line). This is an example of how the effect of the diffusion weighted signal phase can be detected in experiments without the obligation to measure the phase itself, which can be a challenging task (see the discussion below).

VII. DISCUSSION

The main subject of this paper is the detailed analysis of the recently proposed NMR-based diffusion pore imaging technique. While the possibilities of determining the pore structure by diffusion NMR using antisymmetric gradients have been investigated comprehensively, the concept that such NMR diffusion experiments can be interpreted as imaging experiments, which yield the pore space function, was proposed in our recent Letter [35]. The work presented here extends these findings in several regards. Possibly occurring artifacts are considered and a discussion of the diffusion weighted imaginary signal phenomenon—and its relation to properties of the boundary—is presented. Moreover, the $\mathcal{B}$ matrices that were used in the Letter are stated, which allows a convenient reproduction and further investigation of the presented results.

The close analogy of the diffusion pore imaging technique to classical NMR imaging implies that many properties of NMR imaging can be directly translated into diffusion pore imaging. For example, the occurring edge enhancement described in Sec. IV A 2 is a well-known artifact in microscopic NMR imaging [58–62]. Many other properties of NMR imaging, which were not described in the results sections, can also be directly translated: For example, the signal-to-noise ratio must be proportional to the square root of the number of averages, and the signal magnitude can be described by a Rician distribution if real and imaginary part of the signal exhibit Gaussian noise [75].

However, some artifacts do not occur in conventional NMR imaging. For example, the image smearing, as described in Sec. IV A 1, and the possible shift of the image due to a shift of the center of mass $\mathbf{x}_{\text{c.m.},1}$ if surface relaxation is present, are not known from microscopic NMR imaging.

A translation of the diffusion pore imaging technique to real experiments is still lacking. At first instance, phantom experiments could be performed. For example, cylindrical, water-filled capillaries were used by Bar-Shir *et al.* [41] to acquire q-space imaging spectra of high quality. The diameter of these cylinders was in the order of 10 μm, and the application of the pore imaging technique to this phantom appears to be realistic using an NMR spectrometer. A possible alternative is to use hyperpolarized xenon or helium gas [76–78]. Due to the higher gas diffusion coefficient, experiments could also be performed with phantoms of millimeter length, and thus at clinical MR scanners. This requires a hyperpolarization setup and the necessary transmit and receive coils and amplifiers, but benefits from the long transversal relaxation times of gases.

In vivo applications of this approach could have a major impact in clinical imaging. However, the straightforward application of diffusion pore imaging in real tissues is hampered by two complications. First, unlike the assumptions made in this paper, there exists a finite membrane permeability [79]. Second, extracellular fluid is present. The permeability issue could be coped with by restricting oneself to systems of negligible membrane permeability. For example, the permeability of axonal membranes is much lower than that of other cellular membranes due to myelination [8,40,80]. Moreover, certain macromolecules such as N-acetylaspartate are predominantly present inside of cells and thus represent excellent intracellular diffusion markers [81–83]. As we are currently not aware of a straightforward translation of the diffusion pore imaging technique to permeable and open domains, one suitable approach described in the NMR diffusion literature could be followed. Here, the open extracellular compartment is modeled by a spin pool that exhibits a Gaussian phase distribution, for example, by using the composite hindered and restricted model of diffusion (CHARMED) model [84]. This approach allows fitting the extracellular compartment by an exponentially decaying signal attenuation curve, thus possibly allowing to extract detailed information on the

intracellular signal. While the Gaussian phase approximation for the extracellular water may not be fulfilled in all systems, e.g., deviations from Gaussian behavior could be observed in quasiextracellular phantoms [85–87], it may be a good initial approximation. This is particularly true when the motional narrowing approximation is fully valid, implicating the validity of the Gaussian phase approximation. Diffusion pore imaging could be used to test the predictions of such model-based approaches.

Besides these obstacles, a successful application of diffusion pore imaging in real experiments relies on the stable detection of the signal phase. This is difficult due to concomitant fields [88] and strong eddy currents that occur when applying the long and steep diffusion gradients. Specially adapted eddy current compensation schemes, for instance, similar to those proposed by Reese *et al*. [89], must be used. Second, especially if an application *in vivo* is intended, the phase becomes instable due to tissue pulsation, which must be taken into account using elaborate techniques [90,91].

The reward of coping with these obstacles is the greatly increased signal-to-noise ratio. The obtained image in a multipore setup is the average image of all pores, with the signal of all pores added up instead of being distributed over the sample as in microscopic NMR imaging. For instance, if a structure is measured that consists of many similar pores, the individual pore shape (e.g., the shape of an individual lung alveolus) may be of lesser importance than the shape of the average pore. In this case, the diffusion pore imaging technique is well suited to detect that average pore shape.

As shown in this work, it turns out that a much wider class of gradient profiles can be used for the diffusion pore imaging technique than the profile $\mathbf{G}_{t_1,t_2,T}(t)$ that was originally proposed in Ref. [35] [Eqs. (6) and (32)]. The gradient profile must essentially have only two properties in order to be appropriate. First, there must be exactly one sharp gradient pulse that acts as an imaging gradient. This gradient can be placed anywhere in the diffusion weighting: Every particle—so to speak—memorizes its position at the time point of the sharp gradient. Second, the gradient profile must additionally generate a particle phase that compensates for the displacement of the pore if $\mathbf{x}_{\text{c.m.}} \neq 0$. The most forward approach is to use a long, constant, weak gradient. However, almost every long and weak gradient is suitable. Constant weak gradients lead to a better convergence of $\mathbf{x}_{\text{c.m.},1}$, towards $\mathbf{x}_{\text{c.m.}}$, but are not strictly necessary. These observations have two immediate implications. First, shaping the long gradient differently can hardly yield any further information about the domain. But we already know the exact shape of the boundary, thus there is not much more information about the pore that one could be interested in (at least for simple, closed, single length scale pores without permeability, etc.). The second implication, on the other hand, may be a major advantage: The freedom to shape the gradient profile can be used to minimize the mentioned disturbing effects (eddy currents, concomitant fields, etc.). For example, the sharp gradient can be placed before or after 180° pulses. This might be valuable in actual experimental setups.

A recent publication by Shemesh *et al*. indicates that the phase information of the pore space function is also accessible using gradient profiles that consist solely of short gradient pulses [92]. Given these findings, a pivotal remaining question is whether further suitable gradient profiles exist, and which profile is best suited in practice.

Besides the pore imaging approach, the use of nonantisymmetric gradients to detect spatial coherences of pores or cells (see Fig. 11) might be a valuable approach, in particular since cancerous tissue often grows incoherently and disorderedly (see, e.g., Ref. [93] and references therein). Information on spatial coherence could be obtained without sampling the full q space, but only two or three q values. This minimizes the acquisition time, which is an important factor in clinical applications. Moreover, the signal phase needs not to be detected directly, which might render this approach more stable than the diffusion pore imaging technique. Another advantage is that this approach does not rely on the assumption that the pore is closed. In future research, it should be evaluated which additional information can be gained in comparison to other NMR diffusion contrasts, such as the microscopic anisotropy contrast known from double wave-vector experiments [94–98].

The presented $\mathcal{B}$ matrices allow the application of the MCF approach to a class of model domains which are less symmetric than currently available model domains. This is advantageous, since the MCF approach permits much more precise and fast simulations of the diffusion weighted signal attenuation than, for example, Monte Carlo simulations [99]. The model domains could in principle be applied in a broad range of applications, such as the computation of diffusion tensors [100], diffusion kurtosis tensors [32,101], the investigation of temporally oscillating gradients [31,102], or multiple wave-vector experiments [56,94,103]. Especially the phenomenon that the diffusion weighted signal has a nonzero phase is only observable in model geometries of reduced symmetry, and thus the triangular domains are particularly well suited for investigations of this phenomenon.

In conclusion, the shape of closed pores can be measured unambiguously using the diffusion pore imaging technique. The artifacts discussed in this paper are benign and the diffusion gradients can be shaped with a large degree of freedom, so that an experimental implementation should be possible. Such an implementation remains the next crucial step in establishing the diffusion pore imaging technique.

APPENDIX A: EIGENFUNCTIONS OF THE TRIANGLES

We assume $L = 1$.

1. Eigenfunctions and values of the equilateral triangle

The eigenfunctions of the equilateral triangle [Fig. 1(b)] can be separated into those symmetric to the y axis and those antisymmetric to the y axis [104,105]. They are labeled $u_{s;n,k}(\mathbf{r})$ and $u_{a;n,k}(\mathbf{r})$, respectively. Here, n and k are integer numbers indexing the eigenfunctions with $k \geqslant n$ for the symmetric mode and with $k > n$ for the antisymmetric mode:

$$\begin{aligned} u_{s;n,k}(\mathbf{r}) = \beta_{n,k}\{&\cos[2\pi(-k+n)x/3]\cos[2\pi(k+n)y/\sqrt{3}] \\ &+ \cos[2\pi(2k+n)x/3]\cos[2\pi ny/\sqrt{3}] \\ &+ \cos[2\pi(k+2n)x/3]\cos[2\pi ky/\sqrt{3}]\}, \end{aligned} \tag{A1}$$

$$u_{a;n,k}(\mathbf{r}) = \beta_{n,k}\{\sin[2\pi(-k+n)x/3]\cos[2\pi(k+n)y/\sqrt{3}] + \sin[2\pi(2k+n)x/3]\cos[2\pi ny/\sqrt{3}] - \sin[2\pi(k+2n)x/3]\cos[2\pi ky/\sqrt{3}]\}. \quad \text{(A2)}$$

The eigenvalues of the symmetric and antisymmetric modes are identical:

$$\lambda_{s;n,k} = \lambda_{a;n,k} = \lambda_{n,k} = \tfrac{16}{9}\pi^2(n^2+k^2+nk), \quad \text{(A3)}$$

and $\beta_{n,k}$ normalizes the eigenfunctions:

$$\beta_{n,k} = (2\sqrt{4-2\delta_{n,k}})/[3^{3/4}\sqrt{(1+\delta_{0,n}+\delta_{0,k}-2\delta_{0,n}\delta_{0,k})(1+5\delta_{0,n}\delta_{0,k})}]. \quad \text{(A4)}$$

2. Eigenfunctions and values of the hemiequilateral triangle

The eigenfunctions $u_{n,k}(\mathbf{r})$ of the hemiequilateral triangle [Fig. 1(c)] are identical to the eigenfunctions $u_{s;n,k}(\mathbf{r})$ of the equilateral triangle (the antisymmetric mode does not exist) [105]. Thus, the eigenvalues are identical, but in order to guarantee a proper normalization, $\beta_{n,k}$ must be multiplied by $\sqrt{2}$:

$$\beta_{n,k} = \sqrt{2}(2\sqrt{4-2\delta_{n,k}})/[3^{3/4}\sqrt{(1+\delta_{0,n}+\delta_{0,k}-2\delta_{0,n}\delta_{0,k})(1+5\delta_{0,n}\delta_{0,k})}]. \quad \text{(A5)}$$

3. Eigenfunctions and values of the isosceles perpendicular triangle

The eigenfunctions of the isosceles perpendicular triangle [Fig. 1(d)] are

$$u_{n,k}(\mathbf{r}) = \beta_{n,k}[\cos(\pi nx)\cos(\pi ky) + \cos(\pi ny)\cos(\pi kx)], \quad \text{(A6)}$$

with $k \geqslant n$. These are derived from the eigenfunctions of the square. The eigenvalues are

$$\lambda_{n,k} = \pi^2(n^2+k^2), \quad \text{(A7)}$$

and $\beta_{n,k}$ is

$$\beta_{n,k} = \begin{cases} 1/\sqrt{2} & \text{if} \quad n=0 \quad \text{and} \quad n=k, \\ \sqrt{2} & \text{if} \quad n=0 \quad \text{and} \quad n\neq k, \\ \sqrt{2} & \text{if} \quad n>0 \quad \text{and} \quad n=k, \\ 2 & \text{if} \quad n>0 \quad \text{and} \quad n\neq k. \end{cases} \quad \text{(A8)}$$

APPENDIX B: $\mathcal{B}$ MATRICES OF THE TRIANGLES

1. $\mathcal{B}$ matrices of the equilateral triangle

The elements of the $\mathcal{B}$ matrices of the equilateral triangle can be stated as

$$\mathcal{B}^{y,as}_{m_1,n_1;m_2,n_2} = \mathcal{B}^{y,sa}_{m_1,n_1;m_2,n_2} = \mathcal{B}^{x,aa}_{m_1,n_1;m_2,n_2} = \mathcal{B}^{x,ss}_{m_1,n_1;m_2,n_2} = 0, \quad \text{(B1)}$$

$$\mathcal{B}^{y,aa}_{m_1,n_1;m_2,n_2} = -\left(1-\delta_{m_1,n_1}\right)\left(1-\delta_{m_2,n_2}\right)\delta_{m_1,m_2}\delta_{n_1,n_2}\frac{\sqrt{3}}{2} + \beta_{m_1,n_1}\beta_{m_2,n_2}\sum_{i=1}^{18}\frac{81d_{6,i}}{128\pi^3 d_{1,i}}\sum_{j=2}^{5}\frac{\sin\left(\frac{2\pi}{3}d_{j,i}\right)}{d_{j,i}^2}, \quad \text{(B2)}$$

$$\mathcal{B}^{y,ss}_{m_1,n_1;m_2,n_2} = -\delta_{m_1,m_2}\delta_{n_1,n_2}\frac{\sqrt{3}}{2} - \beta_{m_1,n_1}\beta_{m_2,n_2}\sum_{i=1}^{18}\frac{81}{128\pi^3 d_{1,i}}\sum_{j=2}^{5}\frac{\sin\left(\frac{2\pi}{3}d_{j,i}\right)}{d_{j,i}^2}, \quad \text{(B3)}$$

$$\mathcal{B}^{x,as}_{m_1,n_1;m_2,n_2} = -\beta_{m_1,n_1}\beta_{m_2,n_2}\sum_{i=1}^{18}\frac{9\sqrt{3}d_{7,i}}{128\pi^3 d_{1,i}^2}\sum_{j=2}^{5}\frac{(3d_{1,i}+6d_{j,i})\left[1-\cos\left(\frac{2\pi}{3}d_{j,i}\right)\right]-2\pi d_{1,i}d_{j,i}\sin\left(\frac{2\pi}{3}d_{j,i}\right)}{d_{j,i}^2}, \quad \text{(B4)}$$

$$\mathcal{B}^{x,sa}_{m_1,n_1;m_2,n_2} = \mathcal{B}^{x,as}_{m_2,n_2;m_1,n_1}. \quad \text{(B5)}$$

The coefficients $d_{j,i}$ are stated in Table II.

Direct numerical computation of the $\mathcal{B}$ matrices using Eqs. (B2)–(B4) is in general not possible since some $d_{i,j}$ are equal to zero. However, the complete expressions are well defined, and the matrices can be computed by a proper series expansion around $d_{i,j} = 0$. This procedure is somewhat analogous to the numerical computation of $\mathrm{sinc}(x) = \sin(x)/x$ at $x = 0$. The advantage of these expressions over direct numerical integration is twofold: The computation is much faster and numerically more stable. For details, see the Supplemental Material [57].

The notation is as follows: The matrices are labeled by upper indices (e.g., $\mathcal{B}^{y,aa}$) and the elements are labeled by lower indices (e.g., $\mathcal{B}^{y,aa}_{m_1,n_1;m_2,n_2}$). The notation of the indices accompanying $\mathcal{B}$ is as follows: The first upper index (x or y) indicates the gradient

TABLE II. Coefficients for the computation of the $\mathcal{B}$ matrices of the equilateral triangle.

i	$d_{1,i}$	$d_{2,i}$	$d_{3,i}$	$d_{4,i}$	$d_{5,i}$	$d_{6,i}$	$d_{7,i}$
1	$m_1+m_2+2n_1+2n_2$	$-m_1+2m_2+n_1+n_2$	$-m_1-m_2+n_1+n_2$	$2m_1-m_2+n_1+n_2$	$2m_1+2m_2+n_1+n_2$	1	-1
2	$m_1-2m_2-n_1-n_2$	$2m_1-m_2+n_1-2n_2$	$-m_1-m_2-2n_1+n_2$	$2m_1-m_2+n_1+n_2$	$-m_1-m_2-2n_1-2n_2$	1	-1
3	$m_1-2m_2+2n_1-n_2$	$2m_1-m_2+n_1-2n_2$	$-m_1-m_2+n_1+n_2$	$2m_1-m_2+n_1+n_2$	$-m_1-m_2+n_1-2n_2$	1	-1
4	$m_1+m_2-n_1-n_2$	$2m_1-m_2+n_1-2n_2$	$-m_1+2m_2-2n_1+n_2$	$2m_1+2m_2+n_1+n_2$	$-m_1-m_2-2n_1-2n_2$	1	-1
5	$m_1+m_2-n_1+2n_2$	$-m_1+2m_2-2n_1+n_2$	$-m_1-m_2-2n_1+n_2$	$2m_1-m_2+n_1+n_2$	$2m_1+2m_2+n_1+n_2$	1	-1
6	$m_1+m_2+2n_1-n_2$	$2m_1-m_2+n_1-2n_2$	$-m_1+2m_2+n_1+n_2$	$2m_1+2m_2+n_1+n_2$	$-m_1-m_2+n_1-2n_2$	1	-1
7	$2m_1-m_2+n_1-2n_2$	$m_1-2m_2-n_1-n_2$	$m_1+m_2-n_1-n_2$	$m_1-2m_2+2n_1-n_2$	$m_1+m_2+2n_1-n_2$	1	1
8	$2m_1-m_2+n_1+n_2$	$m_1-2m_2-n_1-n_2$	$m_1-2m_2+2n_1-n_2$	$m_1+m_2-n_1+2n_2$	$m_1+m_2+2n_1+2n_2$	1	1
9	$2m_1+2m_2+n_1+n_2$	$m_1+m_2-n_1-n_2$	$m_1+m_2+2n_1-n_2$	$m_1+m_2-n_1+2n_2$	$m_1+m_2+2n_1+2n_2$	1	1
10	$m_1-m_2-n_1+n_2$	$-m_1+m_2-2n_1+2n_2$	$2m_1-2m_2+n_1-n_2$	$-m_1-2m_2-2n_1-n_2$	$2m_1+m_2+n_1+2n_2$	-1	-1
11	$m_1+2m_2-n_1+n_2$	$-m_1+m_2-2n_1+2n_2$	$2m_1+m_2+n_1-n_2$	$-m_1+m_2-2n_1-n_2$	$2m_1+m_2+n_1+2n_2$	-1	-1
12	$m_1-m_2+2n_1+n_2$	$-m_1+m_2+n_1+2n_2$	$2m_1-2m_2+n_1-n_2$	$-m_1-2m_2+n_1-n_2$	$2m_1+m_2+n_1+2n_2$	-1	-1
13	$m_1+2m_2+2n_1+n_2$	$-m_1+m_2+n_1+2n_2$	$2m_1+m_2+n_1-n_2$	$-m_1+m_2+n_1-n_2$	$2m_1+m_2+n_1+2n_2$	-1	-1
14	$m_1-m_2-n_1-2n_2$	$2m_1-2m_2+n_1-n_2$	$2m_1+m_2+n_1-n_2$	$-m_1+m_2-2n_1-n_2$	$-m_1-2m_2-2n_1-n_2$	-1	-1
15	$m_1-m_2+2n_1-2n_2$	$2m_1-2m_2+n_1-n_2$	$2m_1+m_2+n_1-n_2$	$-m_1+m_2+n_1-n_2$	$-m_1-2m_2+n_1-n_2$	-1	-1
16	$2m_1-2m_2+n_1-n_2$	$m_1-m_2-n_1-2n_2$	$m_1-m_2+2n_1-2n_2$	$m_1-m_2-n_1+n_2$	$m_1-m_2+2n_1+n_2$	-1	1
17	$2m_1+m_2+n_1-n_2$	$m_1-m_2-n_1-2n_2$	$m_1-m_2+2n_1-2n_2$	$m_1+2m_2-n_1+n_2$	$m_1+2m_2+2n_1+n_2$	-1	1
18	$2m_1+m_2+n_1+2n_2$	$m_1-m_2-n_1+n_2$	$m_1+2m_2-n_1+n_2$	$m_1-m_2+2n_1+n_2$	$m_1+2m_2+2n_1+n_2$	-1	1

direction. The second upper index indicates the symmetry of the first and second eigenfunction in the integral of Eq. (22). The lower indices m_1,n_1 and m_2,n_2 are the labels of the eigenfunction $u^*_{m_1,n_1}(\mathbf{r})$ and $u_{m_2,n_2}(\mathbf{r})$, respectively. So, for example,

$$\mathcal{B}^{x,as}_{m_1,n_1;m_2,n_2} = \int_\Omega u^*_{a;m_1,n_1}(\mathbf{r}) u_{s;m_2,n_2}(\mathbf{r}) x d\mathbf{r}. \tag{B6}$$

The complete $\mathcal{B}$ matrix is

$$\mathcal{B} = \cos(\theta)\,\mathcal{B}^x + \sin(\theta)\,\mathcal{B}^y, \tag{B7}$$

with

$$\mathcal{B}^x = \begin{pmatrix} \mathcal{B}^{x,ss} & \mathcal{B}^{x,sa} \\ \mathcal{B}^{x,as} & \mathcal{B}^{x,aa} \end{pmatrix} = \begin{pmatrix} 0 & \mathcal{B}^{x,sa} \\ \mathcal{B}^{x,as} & 0 \end{pmatrix}, \tag{B8}$$

$$\mathcal{B}^y = \begin{pmatrix} \mathcal{B}^{y,ss} & \mathcal{B}^{y,sa} \\ \mathcal{B}^{y,as} & \mathcal{B}^{y,aa} \end{pmatrix} = \begin{pmatrix} \mathcal{B}^{y,ss} & 0 \\ 0 & \mathcal{B}^{y,aa} \end{pmatrix}. \tag{B9}$$

θ is the angle between the gradient direction $\mathbf{e}$ and the x axis. The complete eigenvalue matrix is

$$\Lambda = \begin{pmatrix} \Lambda^s & 0 \\ 0 & \Lambda^a \end{pmatrix}, \tag{B10}$$

with $\Lambda^s = \Lambda^a$ and

$$\Lambda^s_{m_1,n_1;m_2,n_2} = \frac{16}{9}\pi^2 \delta_{m_1,m_2}\delta_{n_1,n_2}\left(n_1^2 + m_1^2 + n_1 m_1\right). \tag{B11}$$

The $\mathcal{B}$ matrices of the equilateral triangle are (larger arrays are provided as Supplemental Material [57])

$$\mathcal{B}^{y,aa} = \begin{pmatrix} 0 & 0 & 0 & 0 & 0 & \vdots \\ 0 & -0.730\,419 & 0 & 0.097\,964 & 0.006\,184\,91 & \vdots \\ 0 & 0 & 0 & 0 & 0 & \vdots \\ 0 & 0.097\,964 & 0 & -0.558\,217 & 0.116\,276 & \vdots \\ 0 & 0.006\,184\,91 & 0 & 0.116\,276 & -0.674\,916 & \vdots \\ \cdots & \cdots & \cdots & \cdots & \cdots & \end{pmatrix},$$

$$\mathcal{B}^{y,ss} = \begin{pmatrix} -0.577\,35 & 0.199\,968 & 0 & -0.024\,996 & 0.028\,279\,8 & \vdots \\ 0.199\,968 & -0.424\,281 & 0.159\,192 & 0.097\,964 & -0.006\,184\,91 & \vdots \\ 0 & 0.159\,192 & -0.577\,35 & 0.174\,936 & 0.115\,194 & \vdots \\ -0.024\,996 & 0.097\,964 & 0.174\,936 & -0.596\,484 & 0.116\,276 & \vdots \\ 0.028\,279\,8 & -0.006\,184\,91 & 0.115\,194 & 0.116\,276 & -0.479\,784 & \vdots \\ \cdots & \cdots & \cdots & \cdots & \cdots & \end{pmatrix},$$

$$\mathcal{B}^{x,as} = \begin{pmatrix} 0 & 0 & 0 & 0 & 0 & \vdots \\ 0.199\,968 & -0.153\,069 & 0.159\,192 & -0.097\,964 & 0.006\,184\,91 & \vdots \\ 0 & 0 & 0 & 0 & 0 & \vdots \\ 0.024\,996 & 0.097\,964 & -0.174\,936 & -0.019\,1336 & 0.116\,276 & \vdots \\ 0.028\,279\,8 & 0.006\,184\,91 & 0.115\,194 & -0.116\,276 & -0.097\,5661 & \vdots \\ \cdots & \cdots & \cdots & \cdots & \cdots & \end{pmatrix}.$$

The matrices are sorted with respect to the eigenvalues $\Lambda = \frac{16\pi^2}{9}\mathrm{diag}(0,1,3,4,7,\ldots)$ with $m = (0,0,1,0,1,\ldots)$ and $n = (0,1,1,2,2,\ldots)$. Thus, for example, the element 0.006 184 91 in $\mathcal{B}^{y,aa}$ corresponds to $m_1 = 1, n_1 = 2, m_2 = 0, n_2 = 1$.

2. $\mathcal{B}$ matrices of the hemiequilateral triangle

For the hemiequilateral triangle, only the symmetric modes of the equilateral triangle exist. The $\mathcal{B}$ matrix for a gradient along the x direction is

$$\mathcal{B}^{x}_{m_1,n_1;m_2,n_2} = -\beta_{m_1,n_1}\beta_{m_2,n_2}\sum_{i=1}^{18}\frac{3\sqrt{3}}{32\pi^3 c_{1,i}}\left[\frac{1}{8}\sum_{j=2}^{5}\left(\frac{-2c_{j,i}\pi\cos\left(\frac{2\pi}{3}c_{j,i}\right)+3\sin\left(\frac{2\pi}{3}c_{j,i}\right)}{c_{j,i}^2}\right)\right.$$
$$\left.+\sin(\pi c_{1,i})\sum_{j=6}^{7}\left(\frac{3-3\cos\left(\frac{\pi}{3}c_{j,i}\right)-\pi c_{j,i}\sin\left(\frac{\pi}{3}c_{j,i}\right)}{c_{j,i}^2}\right)\right]. \tag{B12}$$

The coefficients $c_{j,i}$ are stated in Table III. The $\mathcal{B}$ matrix for a gradient along the y direction is identical to $B^{y,ss}_{m_1,n_1;m_2,n_2}$ of the equilateral triangle.

The $\mathcal{B}$ matrix of the hemiequilateral triangle for a diffusion gradient along the x direction is (larger arrays are provided as Supplemental Material [57])

$$\mathcal{B}^{x} = \begin{pmatrix} 0.166\,667 & -0.070\,687\,2 & 0.062\,046\,3 & -0.060\,966\,2 & 0.016\,327\,3 & \vdots \\ -0.070\,687\,2 & 0.134\,722 & -0.098\,067\,9 & 0.022\,785\,8 & 0.002\,399\,55 & \vdots \\ 0.062\,046\,3 & -0.098\,067\,9 & 0.206\,773 & -0.050\,982\,6 & -0.074\,543\,6 & \vdots \\ -0.060\,966\,2 & 0.022\,785\,8 & -0.050\,982\,6 & 0.125\,54 & -0.016\,453\,5 & \vdots \\ 0.016\,327\,3 & 0.002\,399\,55 & -0.074\,543\,6 & -0.016\,453\,5 & 0.173\,694 & \vdots \\ \cdots & \cdots & \cdots & \cdots & \cdots & \end{pmatrix}.$$

3. $\mathcal{B}$ matrices of the isosceles perpendicular triangle

The $\mathcal{B}$ matrices of the isosceles perpendicular triangle are

$$\mathcal{B}^{x}_{m_1,n_1;m_2,n_2} = \beta_{m_1,n_1}\beta_{m_2,n_2}\sum_{i=1}^{8}\frac{1}{8\pi^3 a_{1,i}}\sum_{j=2}^{5}\frac{-a_{j,i}\pi\cos(\pi a_{j,i})+\sin(\pi a_{j,i})}{a_{j,i}^2} \tag{B13}$$

and

$$\mathcal{B}^{y}_{m_1,n_1;m_2,n_2} = -\mathcal{B}^{x}_{m_1,n_1;m_2,n_2}$$
$$+\beta_{m_1,n_1}\beta_{m_2,n_2}\sum_{i=1}^{4}\frac{1}{2\pi^3}\frac{b_{1,i}\cos(\pi b_{2,i})\sin(\pi b_{1,i})-b_{2,i}\cos(\pi b_{1,i})\sin(\pi b_{2,i})}{\left(b_{1,i}^2-b_{2,i}^2\right)}\sum_{j=3}^{4}\frac{\cos(\pi b_{j,i})+\pi b_{j,i}\sin(\pi b_{j,i})-1}{b_{j,i}^2}, \tag{B14}$$

TABLE III. Coefficients for the computation of the $\mathcal{B}$ matrices of the hemiequilateral triangle (x direction).

i	$c_{1,i}$	$c_{2,i}$	$c_{3,i}$	$c_{4,i}$	$c_{5,i}$	$c_{6,i}$	$c_{7,i}$
1	m_1-m_2	$m_1-2m_2-n_1-n_2$	$2m_1-2m_2+n_1-n_2$	$m_1-m_2-n_1+n_2$	$2m_1-m_2+n_1+n_2$	$m_1-m_2+2n_1-2n_2$	$m_1+m_2+2n_1+2n_2$
2	m_1+m_2	$m_1+m_2-n_1-n_2$	$2m_1+m_2+n_1-n_2$	$m_1+2m_2-n_1+n_2$	$2m_1+2m_2+n_1+n_2$	$m_1-m_2+2n_1-2n_2$	$m_1+m_2+2n_1+2n_2$
3	m_1-n_2	$m_1-m_2-n_1-2n_2$	$2m_1-m_2+n_1-2n_2$	$m_1+m_2-n_1-n_2$	$2m_1+m_2+n_1-n_2$	$m_1-2m_2+2n_1-n_2$	$m_1+2m_2+2n_1+n_2$
4	m_1+n_2	$m_1-m_2-n_1+n_2$	$2m_1-m_2+n_1+n_2$	$m_1+m_2-n_1+2n_2$	$2m_1+m_2+n_1+2n_2$	$m_1-2m_2+2n_1-n_2$	$m_1+2m_2+2n_1+n_2$
5	$m_1-m_2-n_2$	$m_1-m_2-n_1-2n_2$	$2m_1-m_2+n_1-2n_2$	$m_1-2m_2-n_1-n_2$	$2m_1-2m_2+n_1-n_2$	$m_1+m_2+2n_1-n_2$	$m_1-m_2+2n_1+n_2$
6	$m_1+m_2+n_2$	$m_1+2m_2-n_1+n_2$	$2m_1+2m_2+n_1+n_2$	$m_1+m_2-n_1+2n_2$	$2m_1+m_2+n_1+2n_2$	$m_1+m_2+2n_1-n_2$	$m_1-m_2+2n_1+n_2$
7	m_2-n_1	$m_1+m_2-n_1-n_2$	$-m_1+2m_2-2n_1+n_2$	$m_1+2m_2-n_1+n_2$	$-m_1+m_2-2n_1-n_2$	$2m_1-m_2+n_1-2n_2$	$2m_1+m_2+n_1+2n_2$
8	m_2+n_1	$-m_1+2m_2+n_1+n_2$	$m_1+m_2+2n_1-n_2$	$-m_1+m_2+n_1-n_2$	$+m_1+2m_2+2n_1+n_2$	$2m_1-m_2+n_1-2n_2$	$2m_1+m_2+n_1+2n_2$
9	n_1-n_2	$m_1-m_2+2n_1-2n_2$	$m_1+m_2+2n_1-n_2$	$-m_1+m_2+n_1-n_2$	$-m_1-m_2+n_1-2n_2$	$2m_1-2m_2+n_1-n_2$	$2m_1+2m_2+n_1+n_2$
10	n_1+n_2	$-m_1+m_2+n_1+2n_2$	$-m_1-m_2+n_1+n_2$	$m_1-m_2+2n_1+n_2$	$m_1+m_2+2n_1+2n_2$	$2m_1-2m_2+n_1-n_2$	$2m_1+2m_2+n_1+n_2$
11	$m_2-n_1+n_2$	$-m_1+m_2-2n_1+2n_2$	$-m_1+2m_2-2n_1+n_2$	$m_1+2m_2-n_1+n_2$	$m_1+m_2-n_1+2n_2$	$2m_1+m_2+n_1-n_2$	$2m_1-m_2+n_1+n_2$
12	$m_2+n_1+n_2$	$-m_1+m_2+n_1+2n_2$	$-m_1+2m_2+n_1+n_2$	$m_1+2m_2+2n_1+n_2$	$m_1+m_2+2n_1+2n_2$	$2m_1+m_2+n_1-n_2$	$2m_1-m_2+n_1+n_2$
13	$m_1-m_2+n_1$	$2m_1-2m_2+n_1-n_2$	$m_1-2m_2+2n_1-n_2$	$2m_1-m_2+n_1+n_2$	$m_1-m_2+2n_1+n_2$	$m_1-m_2-n_1-2n_2$	$m_1+m_2-n_1+2n_2$
14	$m_1+m_2+n_1$	$2m_1+m_2+n_1-n_2$	$m_1+m_2+2n_1-n_2$	$2m_1+2m_2+n_1+n_2$	$m_1+2m_2+2n_1+n_2$	$m_1-m_2-n_1-2n_2$	$m_1+m_2-n_1+2n_2$
15	$m_1+n_1+n_2$	$2m_1-m_2+n_1+n_2$	$m_1-m_2+2n_1+n_2$	$2m_1+m_2+n_1+2n_2$	$m_1+m_2+2n_1+2n_2$	$m_1-2m_2-n_1-n_2$	$m_1+2m_2-n_1+n_2$
16	$m_1+n_1-n_2$	$2m_1-m_2+n_1-2n_2$	$m_1-m_2+2n_1-2n_2$	$2m_1+m_2+n_1-n_2$	$m_1+m_2+2n_1-n_2$	$m_1-2m_2-n_1-n_2$	$m_1+2m_2-n_1+n_2$
17	$m_1+m_2+n_1+n_2$	$2m_1+2m_2+n_1+n_2$	$m_1+2m_2+2n_1+n_2$	$2m_1+m_2+n_1+2n_2$	$m_1+m_2+2n_1+2n_2$	$m_1+m_2-n_1-n_2$	$m_1-m_2-n_1+n_2$
18	$m_1-m_2+n_1-n_2$	$2m_1-m_2+n_1-2n_2$	$m_1-m_2+2n_1-2n_2$	$2m_1-2m_2+n_1-n_2$	$m_1-2m_2+2n_1-n_2$	$m_1+m_2-n_1-n_2$	$m_1-m_2-n_1+n_2$

$$\mathcal{B}^x_{0,0;m,n} = \begin{cases} -2/(n^2\pi^2) & \text{if} \quad m=0 \quad \text{and} \quad n>0, \\ -1/(n^2\pi^2) & \text{if} \quad m=n \quad \text{and} \quad n>0, \\ 2/3 & \text{if} \quad m=0 \quad \text{and} \quad n=0, \\ 0 & \text{otherwise.} \end{cases} \tag{B15}$$

The coefficients $a_{j,i}$ and $b_{j,i}$ are stated in Table IV. The $\mathcal{B}$ matrices of the isosceles triangle are (larger arrays are provided as Supplemental Material [57])

$$\mathcal{B}^x = \begin{pmatrix} 0.666\,667 & -0.202\,642 & -0.101\,321 & 0.050\,660\,6 & 0 & \vdots \\ -0.202\,642 & 0.590\,676 & -0.202\,642 & -0.112\,579 & -0.053\,733\,7 & \vdots \\ -0.101\,321 & -0.202\,642 & 0.704\,662 & -0.101\,321 & -0.159\,211 & \vdots \\ 0.050\,660\,6 & -0.112\,579 & -0.101\,321 & 0.647\,669 & -0.143\,29 & \vdots \\ 0 & -0.053\,733\,7 & -0.159\,211 & -0.143\,29 & 0.642\,04 & \vdots \\ \cdots & \cdots & \cdots & \cdots & \cdots & \end{pmatrix},$$

$$\mathcal{B}^y = \begin{pmatrix} 0.333\,333 & -0.202\,642 & 0.101\,321 & -0.050\,660\,6 & 0 & \vdots \\ -0.202\,642 & 0.409\,324 & -0.202\,642 & -0.112\,579 & 0.053\,733\,7 & \vdots \\ 0.101\,321 & -0.202\,642 & 0.295\,338 & 0.101\,321 & -0.159\,211 & \vdots \\ -0.050\,660\,6 & -0.112\,579 & 0.101\,321 & 0.352\,331 & -0.143\,29 & \vdots \\ 0 & 0.053\,733\,7 & -0.159\,211 & -0.143\,29 & 0.357\,96 & \vdots \\ \cdots & \cdots & \cdots & \cdots & \cdots & \end{pmatrix}.$$

TABLE IV. Coefficients for the computation of the $\mathcal{B}$ matrices of the isosceles perpendicular triangle.

i	$a_{1,i}$	$a_{2,i}$	$a_{3,i}$	$a_{4,i}$	$a_{5,i}$	$b_{1,i}$	$b_{2,i}$	$b_{3,i}$	$b_{4,i}$
1	m_2-n_2	$m_1+m_2-n_1-n_2$	$m_1+m_2+n_1-n_2$	$-m_1+m_2+n_1-n_2$	$-m_1+m_2-n_1-n_2$	m_1	n_1	m_2-n_2	m_2+n_2
2	m_2+n_2	$-m_1+m_2+n_1+n_2$	$-m_1+m_2-n_1+n_2$	$m_1+m_2-n_1+n_2$	$m_1+m_2+n_1+n_2$	m_1	n_2	m_2-n_1	m_2+n_1
3	m_2-n_1	$m_1+m_2-n_1-n_2$	$-m_1+m_2-n_1+n_2$	$m_1+m_2-n_1+n_2$	$-m_1+m_2-n_1-n_2$	m_2	n_1	m_1-n_2	m_1+n_2
4	m_2+n_1	$-m_1+m_2+n_1+n_2$	$m_1+m_2+n_1-n_2$	$-m_1+m_2+n_1-n_2$	$m_1+m_2+n_1+n_2$	m_2	n_2	m_1-n_1	m_1+n_1
5	m_1-n_2	$m_1-m_2-n_1-n_2$	$m_1+m_2-n_1-n_2$	$m_1-m_2+n_1-n_2$	$m_1+m_2+n_1-n_2$				
6	m_1+n_2	$m_1-m_2-n_1+n_2$	$m_1+m_2-n_1+n_2$	$m_1-m_2+n_1+n_2$	$m_1+m_2+n_1+n_2$				
7	m_1-n_1	$m_1-m_2-n_1-n_2$	$m_1+m_2-n_1-n_2$	$m_1-m_2-n_1+n_2$	$m_1+m_2-n_1+n_2$				
8	m_1-n_1	$m_1-m_2+n_1-n_2$	$m_1+m_2+n_1-n_2$	$m_1-m_2+n_1+n_2$	$m_1+m_2+n_1+n_2$				

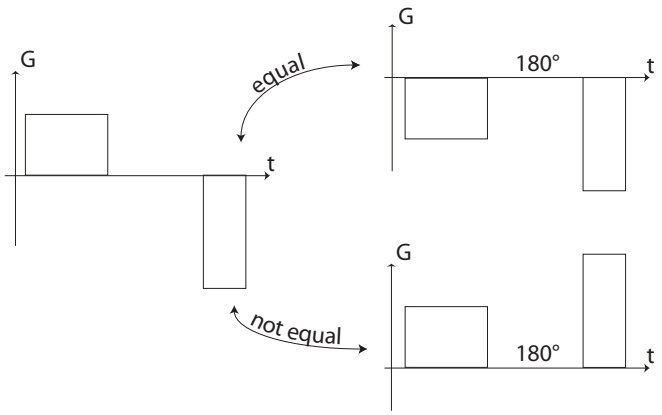

FIG. 12. 180° rf pulses and effective temporal gradient profile. When using temporally asymmetric temporal gradient profiles, the two cases plotted on the right must be distinguished. The second gradient determines the imaginary signal attenuation (in the sense of Sec. II, it is an imaging vector), and thus the upper right gradient profile is equivalent to the left one.

APPENDIX C: GENERATING FUNCTIONAL OF THE ISOSCELES TRIANGLE

In Sec. III, the constant ζ_{-1} appeared describing the width of the center of mass distribution after the first gradient. In this Appendix we state some analytical results describing how this constant (and other ζ constants) of the isosceles triangle can be derived.

Defining the normalized phase $\phi = \varphi/(\gamma GLT)$, the expectation value of the second moment $\langle \frac{\phi^2}{2} \rangle$, e.g., for $f_{0.5,0.5}(\tau)$, can be stated as

$$\left\langle \frac{\phi^2}{2} \right\rangle = \frac{1}{12}\zeta_1 p + \frac{4-\sqrt{2}}{35}\zeta_{3/2} p^{3/2} \tag{C1}$$

in the short time limit and as

$$\left\langle \frac{\phi^2}{2} \right\rangle = \zeta_{-1} p^{-1} - 3\zeta_{-2} p^{-2} \tag{C2}$$

in the long time limit (see Ref. [28] and references therein).

The constants ζ_n [see also Eq. (35)] determine the effect of the boundaries on the second moment and are, e.g., defined by $\zeta_n = \sum_{m=1}^{\infty} \mathcal{B}_{0,m}\lambda_m^n \mathcal{B}_{m,0}$ for $n \leqslant 1$. The function $\mathcal{L}(s) = \sum_{m=1}^{\infty} \frac{\mathcal{B}_{0,m}\mathcal{B}_{m,0}}{s+\lambda_m}$ permits the computation of the ζ constants, e.g., for $k \geqslant 0$, the relation

$$\zeta_{-k-1} = \frac{(-1)^k}{k!}\left(\frac{\partial^k}{\partial s^k}\mathcal{L}(s)\right)_{s=0} \tag{C3}$$

holds true.

Using similar methods as described in Appendix B in Ref. [28], $\mathcal{L}(s)$ can be calculated for the isosceles perpendicular triangle and diffusion gradient along the x direction:

$$\mathcal{L}(s) = -4s^{-3} - s^{-2} + \frac{1}{18}s^{-1} + s^{-5/2}\left(\frac{2}{\tanh(\sqrt{s})} + \frac{\sqrt{2}}{\tanh(\sqrt{s/2})}\right). \tag{C4}$$

Thus, the following numerical values can be retrieved: $\zeta_{-1} = \frac{1}{210}$, $\zeta_{-2} = \frac{17}{37800}$, $\zeta_{-3} = \frac{1}{22680}$, $\zeta_1 = 1$, and $\zeta_{3/2} = \frac{4}{3\sqrt{\pi}}(2+\sqrt{2})$.

APPENDIX D: RELATION BETWEEN PORE SPACE FUNCTION AND $\mathcal{B}$ MATRICES

By interpreting the MCF technique as a description of an NMR imaging experiment, the $\mathcal{B}$ matrices can be related to the pore space function $\chi(\mathbf{r})$. To this end, the time-evolution matrix $\exp[(-D\Lambda + i\gamma G\mathcal{B})T]$ must be considered when diffusion is not present: $\exp[i\gamma G\mathcal{B}T]$. This matrix describes an imaging experiment. In NMR imaging experiments, the signal $S(\mathbf{k})$ is measured, which depends on the image wave vector $\mathbf{k} = \gamma \int \mathbf{G}(t)dt$. Performing a series expansion of $\exp[i\gamma G\mathcal{B}T]$ in G, and of

$$S(\mathbf{k}) = \frac{1}{V}\int_\Omega e^{i\mathbf{k}\cdot\mathbf{x}}d\mathbf{r} = \frac{1}{V}\int_\Omega [1 + i\mathbf{k}\cdot\mathbf{x} - (\mathbf{k}\cdot\mathbf{x})^2 + \cdots]d\mathbf{r} = 1 + is_1 k - \frac{1}{2}s_2 k^2 + O(k^3) \tag{D1}$$

in $k = |\mathbf{k}|$, we find by sorting the terms according to their power in G:

$$B_{0,0} = s_1, \quad \sum_{i=0}^{\infty} B_{0,i}B_{i,0} = s_2, \quad \sum_{i,j=0}^{\infty} B_{0,i}B_{i,j}B_{j,0} = s_3, \text{ etc.},$$

where the s_n constants are the moments of the pore space function $s_n = V^{-1}\int_\Omega (\mathbf{r}\cdot\mathbf{e})^n d\mathbf{r}$, and $\mathbf{e} = \mathbf{k}/k$ is the gradient direction.

APPENDIX E: SPIN ECHOES AND EFFECTIVE TEMPORAL GRADIENT PROFILE

The effect of 180° rf pulses is often taken into account by introducing effective gradient profiles. These are profiles in which the gradient polarity is flipped behind (or before) the 180° pulse. Using temporally antisymmetric profiles, it is irrelevant whether the first or the second gradient is flipped. This is different when using asymmetric temporal profiles (Fig. 12). The last gradient determines the wave vector [Eq. (14)] and thus the first gradient must be flipped. Otherwise the sign of the imaginary signal changes [$\mathrm{Im}(S) \to -\mathrm{Im}(S)$] and the resulting pore images are mirrored.

[1] E. L. Hahn, Phys. Rev. **80**, 580 (1950).
[2] H. Y. Carr and E. M. Purcell, Phys. Rev. **94**, 630 (1954).
[3] E. O. Stejskal and J. E. Tanner, J. Chem. Phys. **42**, 288 (1965).
[4] M. A. Bernstein, K. F. King, and X. J. Zhou, *Handbook of MRI Pulse Sequences* (Elsevier Academic, San Diego, 2004).
[5] P. T. Callaghan, *Principles of Nuclear Magnetic Resonance Microscopy* (Clarendon, Oxford, UK, 1991).
[6] P. C. Lauterbur, Nature (London) **242**, 190 (1973).
[7] E. O. Stejskal, J. Chem. Phys. **43**, 3597 (1965).
[8] H. Johansen-Berg and T. E. J. Behrens, *Diffusion MRI* (Elsevier Academic, London, 2009).

[9] S. Mori, *Introduction to Diffusion Tensor Imaging* (Elsevier Academic, Amsterdam, 2007).
[10] B. Stieltjes *et al*., *Diffusion Tensor Imaging: Introduction and Atlas* (Springer, Berlin, 2012).
[11] T. E. Conturo *et al*., NMR Biomed. **8**, 307 (1995).
[12] S. Mori *et al*., Ann. Neurol. **45**, 265 (1999).
[13] B. Stieltjes *et al*., NeuroImage **14**, 723 (2001).
[14] M. E. Moseley *et al*., Radiology **176**, 439 (1990).
[15] P. J. Basser, J. Mattiello, and D. LeBihan, Biophys. J. **66**, 259 (1994).
[16] T. L. Chenevert, J. A. Brunberg, and J. G. Pipe, Radiology **177**, 401 (1990).
[17] B. M. Ellingson, O. Sulaiman, and S. N. Kurpad, Magn. Reson. Imaging **28**, 1353 (2010).
[18] F. Laun *et al*., Z. Med. Phys. **19**, 11 (2009).
[19] O. Dietrich *et al*., Magn. Reson. Mater. Phys. Biol. Med. **12**, 23 (2001).
[20] J. Zhang *et al*., Magn. Reson. Med. **58**, 454 (2007).
[21] B. Stieltjes *et al*., NeuroImage **31**, 531 (2006).
[22] M. E. Moseley *et al*., Am. J. Neuroradiol. **11**, 423 (1990).
[23] K. O. Lovblad *et al*., Am. J. Neuroradiol. **19**, 201 (1998).
[24] A. Lemke *et al*., Invest. Radiol. **44**, 769 (2009).
[25] T. Yoshikawa *et al*., Am. J. Neuroradiol. **187**, 1521 (2006).
[26] B. Robertson, Phys. Rev. **151**, 273 (1966).
[27] C. H. Neuman, J. Chem. Phys. **60**, 4508 (1974).
[28] D. S. Grebenkov, Rev. Mod. Phys. **79**, 1077 (2007).
[29] P. P. Mitra, P. N. Sen, and L. M. Schwartz, Phys. Rev. B **47**, 8565 (1993).
[30] J. Stepisnik, Physica B **104**, 350 (1981).
[31] M. D. Does, E. C. Parsons, and J. C. Gore, Magn. Reson. Med. **49**, 206 (2003).
[32] J. H. Jensen *et al*., Magn. Reson. Med. **53**, 1432 (2005).
[33] P. T. Callaghan *et al*., Nature (London) **351**, 467 (1991).
[34] D. G. Cory and A. N. Garroway, Magn. Reson. Med. **14**, 435 (1990).
[35] F. B. Laun *et al*., Phys. Rev. Lett. **107**, 048102 (2011).
[36] M. Kac, Am. Math. Mon. **73**, 1 (1966).
[37] C. Gordon, D. L. Webb, and S. Wolpert, Bull. Am. Math. Soc. **27**, 134 (1992).
[38] P. P. Mitra and B. I. Halperin, J. Magn. Reson., Ser. A **113**, 94 (1995).
[39] J. Lätt *et al*., IEEE Transactions on Medical Imaging **26**, 1437 (2007).
[40] Y. Cohen and Y. Assaf, NMR Biomed. **15**, 516 (2002).
[41] A. Bar-Shir *et al*., J. Magn. Reson. **194**, 230 (2008).
[42] P. T. Callaghan *et al*., J. Magn. Reson. **90**, 177 (1990).
[43] R. M. Cotts, Nature (London) **351**, 443 (1991).
[44] D. J. Bergman and K. J. Dunn, Phys. Rev. E **52**, 6516 (1995).
[45] A. Caprihan, L. Z. Wang, and E. Fukushima, J. Magn. Reson., Ser. A **118**, 94 (1996).
[46] P. T. Callaghan, J. Magn. Reson. **129**, 74 (1997).
[47] A. V. Barzykin, J. Magn. Reson. **139**, 342 (1999).
[48] S. Axelrod and P. N. Sen, J. Chem. Phys. **115**, 6878 (2001).
[49] H. C. Torrey, Phys. Rev. **104**, 563 (1956).
[50] W. R. Bauer, C. H. Ziener, and P. M. Jakob, Phys. Rev. A **71**, 053412 (2005).
[51] D. S. Grebenkov, Concepts Magn. Reson., Part A **32A**, 277 (2008).
[52] D. S. Grebenkov, Concepts Magn. Reson., Part A **34A**, 264 (2009).
[53] D. S. Grebenkov, J. Chem. Phys. **126**, 104706 (2007).
[54] D. S. Grebenkov, J. Chem. Phys. **128**, 134702 (2008).
[55] D. S. Grebenkov, J. Magn. Reson. **205**, 181 (2010).
[56] E. Özarslan, N. Shemesh, and P. J. Basser, J. Chem. Phys. **130**, 104702 (2009).
[57] See Supplemental Material at http://link.aps.org/supplemental/10.1103/PhysRevE.86.021906 for the B matrices of the three triangular domains.
[58] T. M. De Swiet, J. Magn. Reson., Ser. B **109**, 12 (1995).
[59] Y. Q. Song *et al*., J. Chem. Phys. **108**, 6233 (1998).
[60] B. Putz, D. Barsky, and K. Schulten, J. Magn. Reson. **97**, 27 (1992).
[61] B. Putz, D. Barsky, and K. Schulten, Chem. Phys. Lett. **183**, 391 (1991).
[62] W. B. Hyslop and P. C. Lauterbur, J. Magn. Reson. **94**, 501 (1991).
[63] C. Beaulieu and P. S. Allen, Magn. Reson. Med. **32**, 579 (1994).
[64] M. Ochs *et al*., Am. J. Respir. Crit. Care. Med. **169**, 120 (2004).
[65] A. C. Wright *et al*., J. Magn. Reson. **186**, 17 (2007).
[66] Z. H. Cho and Y. M. Ro, Magn. Reson. Med. **32**, 258 (1994).
[67] P. M. Heiler *et al*., J. Magn. Reson. Imaging **34**, 935 (2011).
[68] M. D. Robson, D. J. Tyler, and S. Neubauer, Magn. Reson. Med. **53**, 267 (2005).
[69] P. Mansfield, J. Phys. C **10**, L55 (1977).
[70] J. F. Schenck, Med. Phys. **23**, 815 (1996).
[71] T. A. Case *et al*., J. Magn. Reson. **73**, 304 (1987).
[72] P. N. Sen, Concepts Magn. Reson., Part A **23**, 1 (2004).
[73] E. J. Fordham, S. J. Gibbs, and L. D. Hall, Magn. Reson. Imaging **12**, 279 (1994).
[74] M. D. Hurlimann, L. L. Latour, and C. H. Sotak, Magn. Reson. Imaging **12**, 325 (1994).
[75] H. Gudbjartsson and S. Patz, Magn. Reson. Med. **34**, 910 (1995).
[76] X. J. Chen *et al*., Magn. Reson. Med. **42**, 721 (1999).
[77] H. E. Moller *et al*., Magn. Reson. Med. **47**, 1029 (2002).
[78] T. G. Walker and W. Happer, Rev. Mod. Phys. **69**, 629 (1997).
[79] A. L. Sukstanskii, D. A. Yablonskiy, and J. J. Ackerman, J. Magn. Reson. **170**, 56 (2004).
[80] L. Zhao *et al*., NMR Biomed. **21**, 159 (2008).
[81] J. J. Ackerman and J. J. Neil, NMR Biomed. **23**, 725 (2010).
[82] Y. Assaf and Y. Cohen, NMR Biomed. **11**, 67 (1998).
[83] Y. Assaf and Y. Cohen, J. Magn. Reson. **131**, 69 (1998).
[84] Y. Assaf *et al*., Magn. Reson. Med. **52**, 965 (2004).
[85] T. A. Kuder *et al*., Magn. Reson. Med. **67**, 1401 (2012).
[86] F. B. Laun, S. Huff, and B. Stieltjes, Magn. Reson. Imaging **27**, 541 (2009).
[87] E. Fieremans *et al*., J. Magn. Reson. **190**, 189 (2008).
[88] C. Meier *et al*., Magn. Reson. Med. **60**, 128 (2008).
[89] T. G. Reese *et al*., Magn. Reson. Med. **49**, 177 (2003).
[90] C. Liu *et al*., Magn. Reson. Med. **52**, 1388 (2004).
[91] D. C. Karampinos *et al*., Magn. Reson. Med. **62**, 1007 (2009).
[92] N. Shemesh, C. F. Westin, and Y. Cohen, Phys. Rev. Lett. **108**, 058103 (2012).
[93] D. Hanahan and R. A. Weinberg, Cell **144**, 646 (2011).
[94] P. P. Mitra, Phys. Rev. B **51**, 15074 (1995).
[95] E. Ozarslan and P. J. Basser, J. Chem. Phys. **128**, 154511 (2008).
[96] M. E. Komlosh *et al*., Magn. Reson. Med. **59**, 803 (2008).
[97] M. Lawrenz, M. A. Koch, and J. Finsterbusch, J. Magn. Reson. **202**, 43 (2010).

[98] S. N. Jespersen, NMR Biomed. **25**, 813 (2012).
[99] D. S. Grebenkov, J. Magn. Reson. **208**, 243 (2011).
[100] P. J. Basser, and C. Pierpaoli, J. Magn. Reson., Ser. B **111**, 209 (1996).
[101] H. Lu *et al*., NMR Biomed. **19**, 236 (2006).
[102] B. Gross and R. Kosfeld, Messtechnik **77**, 171 (1969).
[103] J. Finsterbusch, J. Magn. Reson. **207**, 274 (2010).
[104] G. Lamé, J. Ecole Polytech. **22**, 194 (1833).
[105] B. J. McCartin, Math. Probl. Eng. **8**, 517 (2002).
[106] J. Ellegood, C. C. Hanstock, and C. Beaulieu, Magn. Reson. Med. **53**, 1025 (2005).
[107] R. W. Mair *et al*., J. Magn. Reson. **135**, 478 (1998).
[108] R. Mills, J. Phys. Chem. **77**, 685 (1973).
[109] M. Ries *et al*., Magn. Reson. Med. **44**, 884 (2000).